Lidar and radar signal simulation: assessment of the stability of the Aerosol-Cloud Interaction index

Author:

Carlos Mario Fajardo Zambrano

BSc. Thesis

In partial fulfillment of the requirements for the degree of:

Physicist Engineer

Supervisor:

PhD. Juan Antonio Bravo Aranda

Co-supervisor:

PhD. Elena Montilla Rosero

Department of Physical Sciences

EAFIT University

Medellín

2020

Agradecimientos

Con el fin de poder alcanzar a todas aquellas personas que hicieron posible de una forma u otra la realización de este trabajo de grado, me tomo la libertad de escribirlo en mi lengua madre. Ademas, quisiera recalcar que mis agradecimientos no solo se limitan a las siguientes líneas, dado que nunca he sido una persona muy dada a expresar sus emociones de forma escrita.

Primeramente, quisiera agradecer a mis padres José y Elizabeth por darme la vida, su apoyo, inculcarme desde pequeño la importancia del esfuerzo propio y el sin fin de lecciones que me han dado a lo largo de la vida (especialmente el forzarme a aprender inglés). A mi hermana Mery, por ser la mejor hermana del mundo, brindándome su apoyo y ayuda (aun cuando no se lo he pedido). A Víctor, mi profesor de física en el colegio, por enseñarme lo maravillosa y atrapante que es la física. A Juan Antonio, no solo por ser el mejor director que exista en la faz de la tierra, sino por ser un gran amigo y tutor, permitiéndome ser un mejor científico y persona. A Elena, por confiar ciegamente en mi y en mis capacidades, permitiéndome cumplir mi sueño de trabajar en el viejo continente. A Manuelita, por ser un gran apoyo en mis múltiples dudas de cómo realizar mi intercambio (aun a costa de su salud). Al grupo de óptica aplicada, especialmente a Camilo y Carlos (aunque ya no se encuentren formalmente en este), quienes me brindaron su apoyo en más de una ocasión, influyendo enormemente en mi formación académica y como persona.

También quisiera gradecer a mis compañeros de carrera, en quienes me apoye en innumerables ocasiones ante los problemas que he tenido que resolver a lo largo de mi formación. A quienes fueron mis compañeros de trabajo en el CEAMA, quienes generan el mejor lugar para trabajar en el mundo por su gran calidez y ayuda (además de ser grandes compañeros de juegos). Y a mis profesores a lo largo de mi carrera, por prepárame a aprender a aprender en este mundo cada vez más cambiante.

Finalizo agradeciendo a todas aquellas personas que impactaron en mayor o menor medida a mi vida (aunque no las mencione en este documento) y me llevaron hasta la culminación de este trabajo de grado.

Content

List of figures

List of tables

Abstract

Aerosol-cloud interaction (ACI) is in the spotlight of the atmosphere science because the low-level knowledge in this process is causing large uncertainties in climate projections. This interaction can be quantified by the aerosol-cloud interaction index (ACI index), which establishes a relationship either between the droplet and aerosol-particle concentration (ACI_{Nd}) or the droplet effective radius and the aerosol-particle concentration (ACI_{reff}). The experimental determination of the ACI index through a synergistic combination of lidar and cloud radar is becoming very difficult due to it requires: first, disentangling the aerosol influence on cloud formation from other influences and, second, retrieving aerosol-particle and cloud microphysics from remote sensing measurements. For a better understanding of the process and to optimize the experimental setup to study the ACI with remote sensing instrumentation, this study presents the LidAr and Radar Signal Simulator (LARSS) used to simulate vertically-resolved lidar and cloud-radar signals during a convective cloud formation (from aerosol hygroscopic growth to condensation droplet growth). By means of LARSS simulations, it has been determined the ACI_{Nd} and ACI_{reff} of several aerosol types (such as ammonium sulfate, burning biomass, and dust), ranging from $ACI_{Nd} = 0.36$ and $ACI_{reff} = 0.12$, for the mixture of all species, and $ACI_{Nd} = 1.00$ and $ACI_{reff} = 0.32$ for coarse-mode dust, with an uncertainty of $6\,\%$ and $5\,\%$ respectively. It has been observed that the ACI index depends on height because the droplet number and effective radius increases with height, reaching a maximum/minimum value when the activation of new droplets stops. The influence in the ACI index due to variations on the updraft velocity, aerosol dry, and wet radius has been studied, concluding that changes in aerosol dry radius cause the greatest influence. Furthermore, it has been defined as a new ACI index, called remote-sensing ACI index (ACI_{Rs}) which presents a linear relationship with the ACI_{reff} depending on the backscatter-related Angstrom exponent. The use of ACI_{Rs} to derive ACI_{reff} may allow quantifying the aerosol-cloud interaction without microphysical inversions

Introduction

For a better understanding of climate change and its future effects, climate projections are required (Ciscar et al., 2009). Thus, atmospheric physical processes need to be deeply investigated. The complexity of the climate system and the multiple interactions inside of it that determine its behavior has produced an incomplete understanding (Solomon et al., 2007). The indirect forcing by aerosols is the overall process by which aerosols influence the earth's radiation balance through the modification of the number of clouds and their albedo (Stocker et al., 2014). These changes occur due to the modification of various variables such as CCN concentration, ice nuclei concentration, water phase partitioning, cloud optical depth, etc., which connect the emission of aerosols with the radiative force of the clouds (Penner et al., 2001).

Consequently, aerosol indirect effects are several, complex, and interlinked since the reduction of the cloud droplet triggers other processes such as, inhibit precipitation (Albrecht, 1989; Rosenfeld, 2000), alters the optical properties, or increase the cloud lifetime (Andreae et al., 2004; Khain et al., 2005). Although many observations are focused on how aerosols influence clouds and their microphysics, conclusions cannot be directly retrieved, since aerosol and clouds can even be interlinked through processes other than physical ACI (Myhre et al., 2007). For example, the aerosol optical depth (AOD) may be affected in the vicinity of the cloud base due to the higher relative humidity presented.

Due to the inability to fully quantify all these effects, the aerosol interaction with clouds is the primary uncertainty on anthropogenic forcing (Change, 2007). Although recent advances have led to a more detailed understanding of ACI, there is still high uncertainty of these processes since the limited observational capabilities and coarse-resolution climate models (Rosenfeld et al., 2014). Making the radiative forcing caused by human activities highly uncertain, and hindering the study of the global warming (Anderson et al., 2003; Stocker et al., 2014).

Feingold et al. (2001) presented the ACI index as a parameter to quantify the influence of aerosols on cloud properties, given by the ratio of cloud optical properties with aerosol optical properties. This index can be retrieved based on in-situ and remote-sensing measurements in three different approaches: purely in situ measurements, combined in situ and remote sensing measurements, and using only remote sensing measurements, presenting a higher correlation for ground-based and aircraft in-situ measurements (Lihavainen et al., 2010; Jia et al., 2019). Aircraft in-situ measurements have proven to be an effective platform for the study of the relationship between aerosols near cloud bases and cloud microphysical properties (Padmakumari et al., 2013; Zhao et al., 2018), facilitating the cloud measurement against ground base in-situ measurement. However, these measurements are expensive, limiting the performed number of aircraft flights.

Despite in-situ experimental approaches have been applied with promising results, these techniques are invasive, being remote-sensing techniques a suitable alternative to retrieve the ACI index in real atmospheric conditions. Sarna and Russchenberg (2016) combined lidar, radar, and microwave radiometer measurements to quantify the ACI index, highlighting the difficulties to disentangle the aerosol influence on clouds from other variables such as temperature or water vapor content. This work presents the simulator LARSS, that reproduces the lidar and radar signals under a convective-cloud formation, to optimize the experimental setup and identify some of the experimental difficulties. LARSS is also used to quantify ACI indexes for different aerosol types and analyse its sensibility to variations of the atmospheric conditions such as dry and wet aerosol modal radius and the updraft velocity.

1. Objectives

1.1. General objective:

Assessment of the ACI index by means of lidar and radar signal theoretical simulations for different aerosol types.

1.2. Specific objectives:

1. Conduct a literature review of the specific physical processes involved to perform a state of the art of the ACI.
2. Comprehend the Hänel and Köhler theories and the droplet condensation growth to implement a program for simulating lidar an radar signals
3. Obtain a simulated lidar and radar signal in function of the particle size distribution (PSD) and droplet size distribution (DSD), respectively, to retrieve the ACI index.
4. Calculate the ACI sensitivity to fluctuations in the aerosol modal radius through the one-variable-at-a-time method, to determine the maximum variations that the PSD may present.
5. Determine the ACI uncertainty trough the Monte Carlo technique to validate the performance of the program.
6. Calculate the ACI index for different aerosol types to optimize the experimental setup.

2. State of art

Although the role of particles as cloud condensation nuclei (CCN) was known already for about a hundred years by Aitken and Wilson (Pruppacher and Klett, 1980; Flossmann and Wobrock, 2010), the aerosol and cloud physics areas have been separate study fields until the 1980s. The first attempt of the relation between aerosols and cloud was the hail prevention by the influence of silver iodide on the formation of the ice phase (Cotton and Pielke Sr, 2007); while the first model made to retrieve the influence of aerosol on the formation and evolution of the cloud was designed in the 80s, allowing the study of the role of particles in the formation and cleaning capacity of clouds in the overall pollution problem. The interest in the relation of aerosol and clouds has been in increase due to the increasing environmental problems with its associated socioeconomic impact such as acid rain and the nuclear winter (Flossmann and Wobrock, 2010).

The ACI is the process that was first theorized by Twomey (1977), who evidenced that an increase of aerosols (who acts as CCN) changes the cloud droplet size distribution and increase the cloud albedo (considering a constant liquid water content) (Costantino and Bréon, 2010). The first quantification of the aerosol cloud interaction was presented by Feingold et al. (2003), as a linear relationship between the logarithm of the cloud droplet effective radius and the logarithm of the aerosol index for a constant liquid water path (LWP).

Numerous studies agree with the Twomey effect for polluted regions in comparison to less polluted cases (Radke et al., 1989; Kaufman and Fraser, 1997; Rosenfeld, 1999). For example, Bréon et al. (2002) presents a negative relationship between cloud droplet radius and the aerosol optical depth, demonstrating the impact of fine-scale aerosol on cloud microphysics, being uncertain the relative altitude levels of aerosols and clouds. Costantino and Bréon (2010) show that aerosol and clouds present a strong(null) correlation when aerosol and cloud layers are mixed(clearly separated), although, a recent study

evidenced that the cloud droplet effective radius varies with the aerosol load as a function of the ambient conditions (Yuan et al., 2008). Also, Liu and Daum (2002) shows an increase in both the relative dispersion and the droplet concentration, being the two effect counteracting, in polluted regions, leading to a smaller cooling effect by aerosols.

Aerosol also affects the cloud cover. For example, Kaufman et al. (2005) shows a strong correlation among aerosol loading, cloud cover, and cloud height, using satellite measurements. Koren et al. (2005), Devasthale et al. (2005) and Kaufman and Koren (2006) presents similar results over the Atlantic Ocean, Europe, and independent geographical locations, respectively. The influence of aerosol on cloud cover is not linear, since an increase of the aerosol load can dramatically increase the cloud cover in ultraclean regions, causing a large cooling (Ackerman et al., 1993; Rosenfeld et al., 2014). It is worthy to note that Myhre et al. (2007) found that most of the strong increase in cloud cover with AOD is due to ACI and a prolonged cloud lifetime. Also, Rosenfeld et al. (2006) shows that cloud cover suffers a greater change for situations with a relatively small amount of aerosols.

The semi-direct aerosol effect is assumed as the effect of absorbing aerosols, causing the evaporation of existing clouds, and blocking surface heating, inhibiting convection and cloud formation (Myhre et al., 2007). This effect is hypothesized that it presents a strong impact on the radiative balance, being especially sensitive to the vertical distribution of aerosols and clouds (Johnson et al., 2004; Penner et al., 2003). Recently, the inhibition of cloud formation has been specially investigated within the semi-direct aerosol effect (Ackerman et al., 2000; Cook and Highwood, 2004; Johnson et al., 2004). Kaufman et al. (2005), and Koren et al. (2005) showed that smoke or pollution each enhances the cloud formation and the cloud top height over the Atlantic Ocean. Jin and Shepherd (2008) evidenced that aerosols may have more effects on cloud formation than convective rainfall, being these effect more frequents over the ocean than overland.

The influence of aerosols in the rainfall is one of the most important and uncertain effects of anthropogenic climate change (Hobbs, 1993). It has been calculated, through different models, that an increase of CCN concentration leads to a drastic decrease in precipitation (Khain et al., 1999; Cui et al., 2006). In a moist unstable atmosphere Teller and Levin (2006), and Fan et al. (2007) obtain that pollution aerosols may invigorate convective clouds and produce more precipitation. However, Khain et al. (2005) showed that an increase in the aerosol load can both decrease and increase precipitation as a function of the environmental conditions. Zhang et al. (2007) presents that polluted aerosols from the Asian continent may significantly impact the global general circulation and climate through the intensification of storms over the Pacific. Goren and Rosenfeld (2012) shows that clouds may be hypersensitive to aerosols that have become extremely depleted by precipitation. Li et al. (2007) evidence that an increase in the aerosol load increases the precipitation from clean maritime to continental background conditions. However, it is considerably reduced or suppressed for under highly polluted conditions, indicating different effects on precipitation efficiency under different aerosol conditions.

Thus, although several measurements and model simulations show the influence of aerosol on cloud formation and microphysics, the magnitude or direction of the effect of aerosols on clouds and its variations with meteorological conditions have not been clearly identified (Levin and Cotton, 2008).

3. Theoretical basis

This section provides the basic concepts of the atmospheric thermodynamic phenomena related to the cloud formation.

3.1. Atmospheric thermodynamics

3.1.1. Temperature lapse rate

Almost all weather phenomena occur in the Troposphere. This first layer of the atmosphere is characterized by a temperature decrease with height with a dry adiabatic lapse rate (γ) of $6.5^{o}C/km$ (Zhang and Moore, 2014; Cavcar, 2000). Thus, the temperature (T) at a height z is generally given by,

$$T(z) = T_o - \gamma(z - z_o) \tag{1}$$

where z_o is the reference height and T_o is the reference temperature at z_o.

3.1.2. Dry and wet adiabatic lapse rate

Vertical movements of air parcels are adiabatic, i.e., without exchanging energy with the environment. If the air parcel is dry (RH$< 100\,\%$), it presents the dry γ. For a saturated air mass parcel (RH$\geq 100\,\%$), the variation of the temperature is given by the wet lapse rate (Γ_s) as a function of pressure and temperature. This change is produced by the condensation of droplets in the saturated air mass, releasing latent heat which reduces the lapse rate (i.e., $\Gamma_s \leq \gamma$) (Wallace and Hobbs, 2006), being expressed by,

$$\Gamma_s = \frac{g}{c_p} \frac{\left(\frac{L_w \mu_s}{R_a T} + 1\right)}{\left(\frac{L_w^2 \mu_s}{c_p R_v T^2} + 1\right)} \tag{2}$$

Where g is the mean gravitational acceleration, c_p is the specific heat capacity of dry air at constant pressure, L_w is the latent heat of water, μ_s is the saturation water vapor mixing ratio, R_a is the specific gas constant of most air, and R_v is the specific gas constant of water vapor (Zhang and Moore, 2014).

3.1.3. Barometric formula

The decrease of pressure with height can be parameterized by the barometric formula,

$$e(z) = e_o \exp\left(\frac{-gM_s}{R_a}\int_0^z \frac{1}{T(s)}ds\right) \tag{3}$$

which describes the pressure trend depending on height z, where e_o is the reference pressure and M_s is the average molar mass of atmospheric gases. Substituting Eq 1 in Eq 3, the barometric formula for linear temperature decrease (Fässler, 2019) is given by,

$$e(z) = e_o\left(1 - \frac{\gamma(z - z_o)}{T_o}\right)^{\frac{g}{\gamma R_a}} \tag{4}$$

3.1.4. Relative humidity

The water vapor mixing ratio is defined by,

$$\mu = \frac{m_v}{m_d} \tag{5}$$

where m_v is the mass of water vapor, and m_d is the mass of the dry air (Zhang and Moore, 2014). On the other hand, if the volume of air is saturated, the μ becomes the μ_s. Considering that the water vapor and dry air both obey the ideal gas equation, the μ_s can be calculated (in hPa) as,

$$\mu_s = 622\frac{e_s}{p - e_s} \tag{6}$$

where e_s is the saturation water-vapor pressure. The ratio between the μ and the μ_s at the same temperature and pressure is known as relative humidity (RH),

$$\text{RH} = 100\,\% \cdot \frac{\mu}{\mu_s} \tag{7}$$

Figure 1 shows T, e, μ_s and RH simulated profiles below the cloud base height (CBH), assuming no other clouds below $3.5km$. From $T_o = 298K$ and $e_o = 101kPa$ the T and e profiles are calculated according to Eq 1 and Eq 4. RH is retrieved form the μ_s profile calculated as a function of e and assuming a constant water vapor content $\mu = 0.67kPa$.

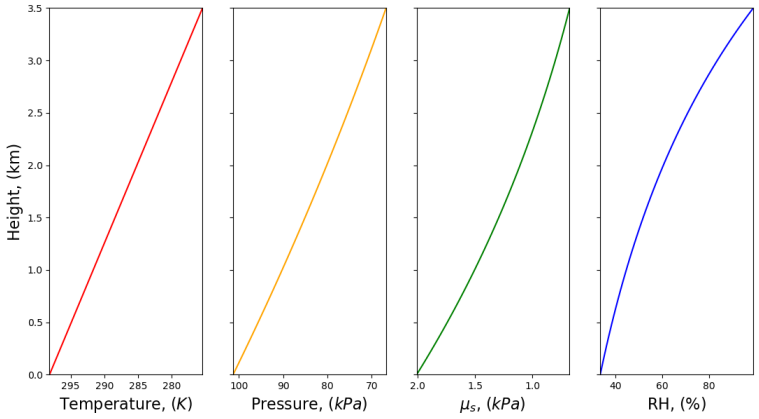

Figure 1. Temperature, pressure, saturation mixing ratio (μ_s) and relative humidity (RH) profiles below the CBH.

3.1.5. Clausius–Clapeyron equation

The Clausius-Caperion equation describes the change of e_s between two phases of matter. For an air parcel, it characterizes the transition from the subsaturated to the supersaturated phase in terms of the water-vapor saturation ratio (S), described by (Koutsoyiannis, 2012),

$$\ln S = \ln \frac{e}{e_s} = \frac{L_w}{R_v}\left(\frac{1}{T_o} - \frac{1}{T}\right) \tag{8}$$

This equation evidences that the amount of water an air mass can store decreases with temperature decrease. Since the amount of water in a given air mass parcel remains constant (absence of precipitation), a temperature decrease large enough may generate an excess of water in the air mass, reaching a supersaturation (SS) state ($SS = (S-1)100\,\%$), i.e., RH $> 100\,\%$ (Koutsoyiannis, 2012; Yau and Rogers, 1996).

Due to Clausius-Caperion equation complexity, a series of approximations have emerged for describing μ_s in a determined interval. Magnus-type equation is one of these approximations, derived from experimental study, which parametrizes e_s (in hPa) between -40^oC and 50^oC (Koutsoyiannis, 2012),

$$e_s(z) = 6.1094 \exp\left(\frac{17.625T(z)}{243.04 + T(z)}\right) \tag{9}$$

3.2. Atmospheric aerosol

Atmospheric aerosols are solid or liquid particles suspended in the atmosphere. These are naturally or anthropologically produced, being its chemical composition strongly related to its source (Chin and Kahn, 2009; Ramachandran, 2018). Depending on their size, aerosols can be classified as Aitken-mode ($0.001\mu m < r < 0.1\mu m$), accumulation-mode ($0.1\mu m < r < 1.0\mu m$) and coarse-mode ($r > 1.0\mu m$) aerosols (see Figure 2). Aitken-mode aerosols are formed by nucleation processes. Accumulation-mode aerosols are formed mostly through the gas-to-particle conversion process, and coarse-mode aerosols are formed directly by mechanical processes such as pollen grains, volcanic emissions, windblown dust, etc. (Ramachandran, 2018).

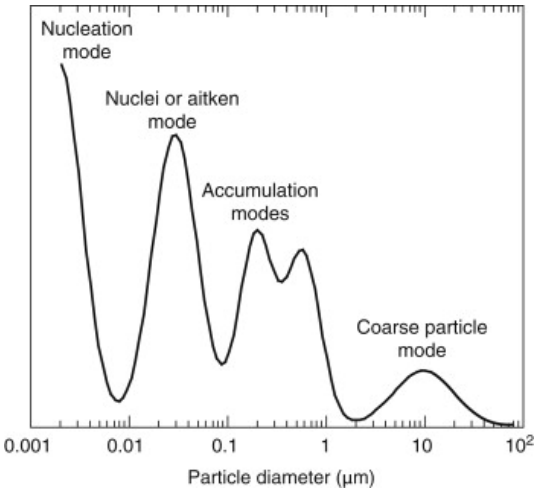

Figure 2. Aerosol size distribution modes (Ernst and Ernst, 2000).

Aerosols present a wide range of different types based on their composition, size, shape, and optical properties (Chin and Kahn, 2009). These are usually characterized by its number concentration (N_a) or mass concentration and the particle size distribution (PSD), which defines the relative amount of particles present according to its size (Jillavenkatesa et al., 2001).

3.2.1. Hänel theory

Aerosol particles could take up water from the atmosphere, growing in size with RH (Hänel, 1976). This process, known as hygroscopic growth, is described by Charlson et al. (1992) as,

$$\frac{A_{\text{wet}}\,(\text{RH})}{A_{\text{dry}}} = \left(1 + \kappa \cdot \frac{\text{RH}}{1 - \text{RH}}\right)^{\frac{1}{3}} \tag{10}$$

where A_{dry} is the diameter of the aerosol at dry RH (RH $< 30\,\%$), A_{wet} is the diameter of the wet aerosol and κ is the hygroscopicity parameter which depends on the aerosol physiochemical properties (Zieger et al., 2013). κ ranges from 0.001 (insoluble minerals) (Sullivan et al., 2009) to 1.16 (sea salt) (Petters and Kreidenweis, 2007). Table 1 shows some κ values for different aerosol types.

Aerosol types	κ
Insoluble minerals	0.001
Black carbon	0.1
Organic carbon	0.14
Dust	0.14
Burning biomass	0.22
Sulfate	0.24
Ammonium sulfate	0.51
Sea salt	1.16

Table 1. κ parameter for different aerosol types (Sullivan et al., 2009; Wu et al., 2019; Psichoudaki et al., 2018; Hande et al., 2016).

Figure 3 shows the hygroscopic growth of the PSD with RH. It is worthy to note that the hygroscopic growth is not linear, presenting larger growth in the RH range 89-99 % than in the RH range 33-88 %.

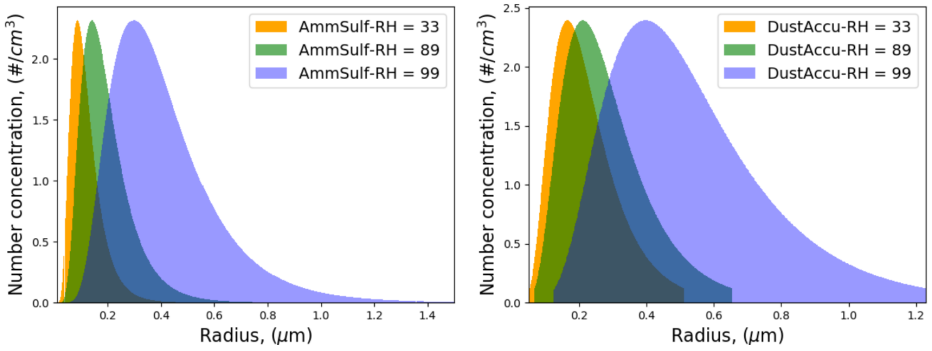

Figure 3. Accumulation-mode ammonium sulfate (left) and dust (rigth) hygroscopic growth.

Eq 10 can parametrize the growth of aerosols up to $RH = 99$. From this point, Hänel parameterization becomes unstable. From $RH \geq 100$ the process is described by the Köhler theory (Yau and Rogers, 1996), presented in the next subsection.

3.2.2. Köhler theory

The Köhler theory is based on both the Solute and Kelvin effects: Solute effect describes how e_s decreases due to the condensation of water in the aerosol surface

whereas Kelvin effect describes how saturation pressure (e_s) increases due to the larger droplet surface tension. Both effects are then opposites (Köhler, 1936; D'Almeida et al., 1991). Based on the Köhler theory, the S over a droplet can be calculated from,

$$S(D) = \frac{d^3 - A_{dry}^3}{d^3 - A_{dry}^3\,(1-\kappa)} \exp\left(\frac{4\sigma_{s/a} M_w}{RT\rho_w d}\right) \tag{11}$$

where d is the wet diameter, $\sigma_{s/a}$ is the surface tension of the solution/air surface, M_w is the molecular weight of water, and ρ_w is the water density. This equation applies from the subsaturated to the supersaturated phases (Petters and Kreidenweis, 2007). Figure 4 shows the S curves for different dry diameters of $NaCl$ aerosol particles. It describes aerosol growth until it reaches the critical supersaturation (SS_{cr}). From this point, the particle is in unstable equilibrium state with its environment, it starts to condensate water, and it is considered as a droplet (Pruppacher and Klett, 1980). Where SS_{cr} is the peak of S curve, being higher(lower) for the smallest(biggest) dry diameters (Zieger et al., 2013).

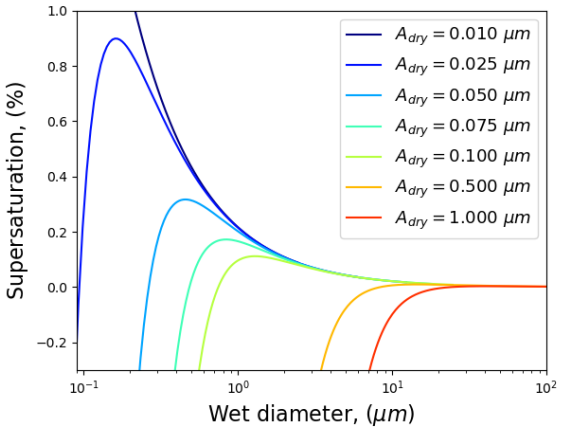

Figure 4. Köhler curves for $NaCl$ particles with different dry diameters at $293K$.

Based on Eq 11, Fitzgerald et al. (1982); Fitzgerald and Hoppel (1984) propose a simplified version as follows,

$$\ln\left(\frac{e}{e_s}\right) = \frac{A}{d} - \frac{B}{d^3} \tag{12}$$

where A and B can be approximated to $A \approx 3.3x10^{-5}/T$ and $B \approx 4.3m_s/M_s$, where m_s and M_s are the mass and molecular mass of the solute, respectively. From the Eq 12, SS_{cr} can be expressed as,

$$SS_{cr} = \exp\left(\sqrt{\frac{4A^3}{27\kappa A_{dry}^3}}\right) \tag{13}$$

This approximation, based on the assumption that κ and B are equivalent, is valid for $SS_{cr} < 1$ and $\kappa > 0.2$.

3.2.3. CCN and interstitial aerosol particles

Under given atmospheric conditions, the aerosol particles that are capable, for its size and hygroscopicity, of initiating droplet formation are called cloud condensation nuclei (CCN) (Pruppacher and Klett, 1980). Since all aerosols are eventually able to become CCN, the activation potential of aerosol can be characterized with the help of the activation fraction (AF), which is the ratio of the CCN and the aerosol number concentration (N_a) (Kalivitis et al., 2015).

$$AF = \frac{CCN}{N_a} \tag{14}$$

The CCN parametrization is a subject of interest since it influences the average size of the droplets, the colloidal stability, and the optical density of the cloud (Twomey and Wojciechowski, 1969). Although all aerosol particles are eventually able to act as CCN, not all particles can be activated, e.g., particles smaller than $0.1\mu m$ would require higher SS than those found on the atmosphere (Yau and Rogers, 1996). The remaining not activated aerosols are called interstitial aerosol. The activated

CCN would continue to grow as long as $RH \geq 100$. Only if air reaches $RH < 100$, the activated CCN would start to evaporate (Verheggen et al., 2007).

3.3. Clouds

Clouds are formed by the activation of aerosol profiles when RH exceeds $100\,\%$ (Wang, 2013). Its microphysical properties depend on cloud droplet nucleation activity, condensation growth of droplets (Chapter 3.3.1), entrainment-mixing processes with environmental drier air at cloud top, and collision-coalescence growth (Pawlowska et al., 2006). According to Miles et al. (2000), the DSD can be adequately modeled by a single-mode gamma or log-normal size distribution with long tails at larger particle sizes. In this case, the DSD is described by,

$$n_d(D_r) = \frac{1}{\sqrt{2\pi}} \frac{N_d}{\ln \sigma} \frac{1}{D_r} \exp\left[-\frac{1}{2}\left(\frac{\ln D_r - \ln D_{rmod}}{\ln \sigma}\right)^2\right] \tag{15}$$

where σ is the standard deviation, D_r is the droplet radius, D_{rmod} is the droplet modal radius, N_d is the total droplet number concentration, and $n_d(D_r)$ is the number of droplets with a D_r.

3.3.1. Condensation growth

Once SS_{cr} is reached, droplets grow in size taking water molecules from surrounding air. This growth continues while $SS > 0$, even for SS lower than SS_{cr}, and it is described in function of the time by the equation,

$$D_r(t) = \sqrt{D_{ro}^2 + 2SS \cdot Q \cdot t} \tag{16}$$

where D_{ro} is the initial droplet radius, t is the time from the droplet activation, and Q is a constant associated with the heat conduction and vapor diffusion of the air parcel (Yau and Rogers, 1996). It can be seen in Eq 16 that condensation growth ($D_r^2 - D_{ro}^2$) is independent of the droplet size. Thus, smaller droplets present a greater relative growth compared to larger droplets, generating a narrowing of the DSD.

Condensation growth of the droplets dominates until they reach a radius of $20\mu m$. From this size, its collision cross-sections and settling speeds are big enough to generate collision-coalescence growth, due to the increasing chance of colliding with each other (Yau and Rogers, 1996).

3.4. Supersaturation

Once SS is reached in a given air parcel, there is a compromise in updraft air parcels between the increase of SS due to temperature decreases with height and the decrease of SS due to condensation. This behavior is described by the following equation (Pinsky et al., 2014),

$$SS = A_1 z_c - A_2 q_w + C \tag{17}$$

where A_1 and A_2 are constants, z_c is the height from the cloud base, C is the initial SS condition, and q_w is the liquid water mixing ratio, which is given by the Eq 18,

$$q_w(t) = \frac{4\pi\rho_w}{3\rho_a} \int_0^\infty D_r(t)^3 n_d(D_r, t) dD_r \tag{18}$$

where ρ_w is the water density and ρ_a is the air density. Figure 5 shows the temperature and pressure profile inside the cloud. From these profiles, the SS is calculated according to the Eq 17.

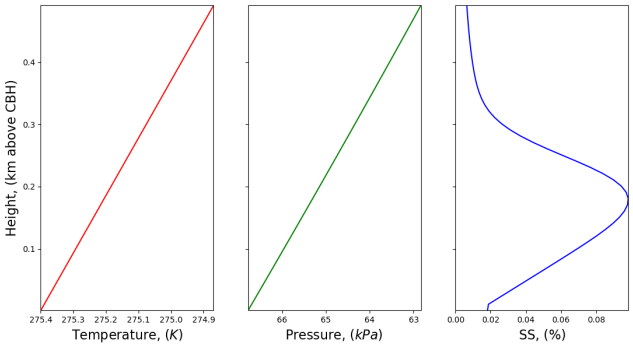

Figure 5. Temperature, pressure and supersaturation profile inside the cloud.

3.5. Aerosol-Cloud Interaction (ACI)

The term aerosol-cloud interaction is defined as the impact of the aerosol on the cloud albedo or first indirect effect. This relationship was postulated by Twomey (1977), who evidenced that the increase in the number of aerosols generates an increase in the droplet number produced but with a smaller size, maintaining larger LWP and generating more reflective clouds and generally less precipitation (Feingold et al., 2001), this process is schematized in Figure 6.

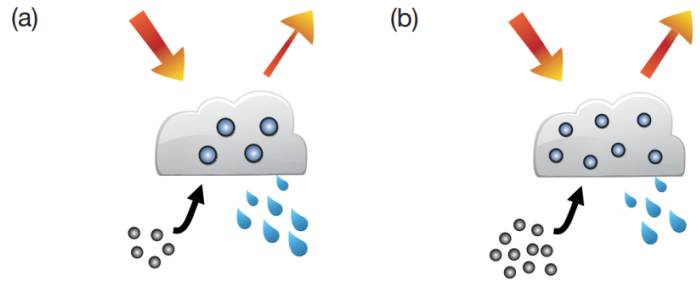

Figure 6. Aerosol-cloud first indirect effect. Panels (a) and (b) represent a clean and a polluted low-level cloud, respectively. Modified from Boucher et al. (2013).

Feingold et al. (2001) introduces the relations to quantify the aerosol-cloud interaction, later referred to as the ACI index. These are given as the ratio between

cloud and aerosol proxies of their microphysics as,

$$
\begin{aligned}
ACI_{reff} &= -\left.\frac{\partial \ln D_{reff}}{\partial \ln \alpha}\right|_{\text{LWP}} \quad 0 < ACI_{reff} < 0.33 \\
ACI_{N_d} &= \frac{\partial \ln N_d}{\partial \ln \alpha} \quad 0 < ACI_{N_d} < 1 \\
ACI_{reff} &= \frac{1}{3} ACI_{Nd}
\end{aligned}
\tag{19}
$$

where D_{reff} is the droplet effective radius, N_d is the droplet number concentration, and α is an N_a proxy, such as extinction (α_{ext}) and backscatter coefficient (β).

4. Experimental setup: remote sensing for studying aerosol-cloud interaction

Remote sensing instrumentation is been used for ACI study from the properties retrieved from lidar and radar according to Eq 19. This section presents the basis of the lidar, radar, and a new measurement of the ACI index based on the optical properties.

4.1. Lidar technique

Lidar, an acronym of *light detection and ranging*, is a remote-sensing instrument to determine aerosol-particle optical properties such as β and α_{ext}, and they typically cover from first hundreds meters until low stratosphere (North et al., 2014). Assuming a monostatic single-wavelength pulsed Lidar, the single-scattering Lidar equation is defined by (Klett, 1981).

$$P(z) = \frac{K}{z^2}\beta(z)T_r^2(z) = \frac{K}{z^2}\beta_{att} \tag{20}$$

where P is the signal received by the Lidar from a distance z; K and z^2 are the performance of the Lidar system and the range-dependent measurement geometry, factors completely determined by the Lidar setup, so these can be manipulated by the user, or remain constant, $\beta(z)$ is the backscatter coefficient, which is the percentage of backward scattered radiation, $T_r(z)$ is the transmission term, which describes the amount of radiation lost due to attenuation in the laser path (explained in Sect. 4.1.1), and β_{att} is the backscatter attenuated coefficient (Weitkamp, 2006).

4.1.1. Transmittance

The Beer–Lambert-Bouger's law describes the total extinction of the collimated light beam in a turbid heterogeneous medium as (Kovalev and Eichinger, 2004):

$$P(z) = P_0 T_r(z) = P_0 e^{-\mathrm{AOD}} \tag{21}$$

where P_0 is the intensity of light before entering the medium, and the aerosol optical depth (AOD) is given by,

$$\mathrm{AOD} = \int_0^z \alpha_{ext}(z')\mathrm{d}z' \tag{22}$$

$$\alpha_{ext} = \int_{r_1}^{r_2} Q_{ext}(m,x)n(r)\pi r^2 dr \tag{23}$$

where α_{ext} is the extinction coefficient described as the fraction of energy removed per unit path length from an incident wave with an energy flux density of one and Q_{ext} is the extinction efficiency which is greatly affected by the size of the particles, so that for large particles $Q_{ext} \to 2$, whereas for small particles this values is much more small (Ramachandran, 2018); m is the real part of the refractive index, $x = 2\pi r/\lambda$ is the size parameter, $n(r)$ is the number of aerosols with radius r, and r_1, r_2 are the boundaries of the PSD.

4.2. Radar measurement

One of the first remote sensing developed techniques was Radio Detection And Ranging (Radar), which works according to the echo-sounding principle (Raghavan, 2013a). There are two different types of radar depending on their target, the cloud radar, and the rain radar. However, in both cases, the reflectivity factor is one of the measurements done by this system. In the case of Mie scattering, i.e. elastic scattering theory applied to particles whose diameter is larger than the wavelength

of the incident radiation, the radar reflectivity factor (Z_e) is given by,

$$Z_e = \frac{\lambda_r^4}{\pi^5 \left|K_p\right|^2} \int \sigma_b(D_d) n(D_d) dD \tag{24}$$

where D_d is the droplet diameter, σ_b is the cross-section of a droplet with diameter D_d, $n(D_d)$ is the number of droplets with diameter D_d, λ_r is the radar wavelength, and $|K_p|^2$ is the dieletric factor (Bringi and Chandrasekar, 2001).

4.3. MOPSMAP

Remote sensing measurements use inversion techniques to retrieve microphysical properties from the optical properties. These inversions are made through optical modeling. Since optical modeling may require long computational time, pre-calculate optical properties are often used. Thus, to retrieve the lidar signal, an open-source software based on a data set of pre-calculated single-particle optical properties called MOPSMAP is used. MOPSMAP (Modeled optical properties of ensembles of aerosol particles) allows retrieving optical properties from PSD, according to either Rayleigh, Mie, T-matrix, or optical-geometry scattering (Gasteiger and Wiegner, 2018).

4.4. ACI remote sensing

As was described in subsection 3.5, ACI indexes are calculated with microphysical properties that require some assumptions. Thereby, to reduce the uncertainties eliminating these assumptions, in this work a new ACI index based on the optical properties retrieved by the lidar and radar is proposed.

$$ACI_{Rs} = -\left.\frac{\partial \ln Z_e}{\partial \ln \beta}\right|_{\mathrm{LWP}} \qquad 0 < ACI_{Rs} < 1 \tag{25}$$

where β is used as a proxy of N_a and Z_e as a proxy of N_d.

5. Lidar And Radar Signal Simulator (LARSS)

LARSS is a tool that has been developed to retrieve ACI indexes from lidar and radar signals under a convective cloud formation. LARSS performance, notation, and the estimation of ACI indexes uncertainties are explained in this section.

5.1. LARSS performance

The simulation starts with an air parcel (with an initial temperature, pressure, and water vapor content) at ground level and typical dry RH in the atmosphere ($RH \approx 30\,\%$) to originate convective clouds, as it is schematized in Figure 7. This air parcel contains aerosol particles which are characterized by its density, hygroscopicity parameter, refractive index, N_a, and by its PSD. The PSD is assumed to be Gaussian, defined by a modal radius, standard deviation, and both minimum and maximum radius.

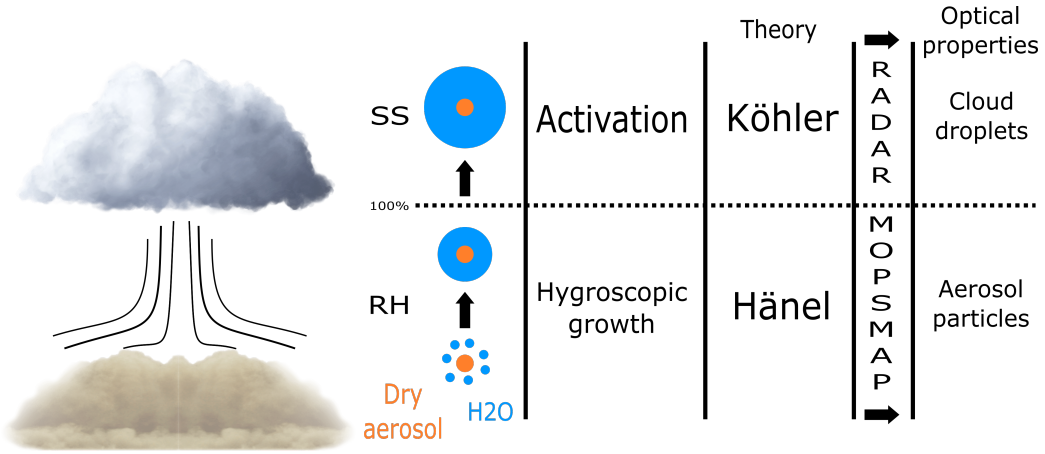

Figure 7. Simulation scheme (left to rigt columns): ascent of dry air parcel, cloud formation, atmospheric process and theories, retrieval of aerosol and cloud optical properties from the PSD and DSD, respectively; and generation of lidar (aerosol and cloud) and radar (cloud) signals

The air-parcel ascent at a given updraft velocity (w) causes the reduction of the temperature and the saturation pressure with height according to the Eq 1 and Eq 9, increasing the RH (see Figure 8 a). The RH increase gives rise to two processes:

the aerosol hygroscopic growth when RH below $100\,\%$ (see Figure 8 b), described by Hänel theory (Hänel, 1976; Zieger et al., 2013), and droplet formation once the SS is reached ($RH \geq 100\,\%$), described by Köhler (Köhler, 1936; Petters and Kreidenweis, 2007). Recalling the subsection 3.2.3, Köhler theory is required once the air parcel reaches the SS since Hänel parameterization becomes unstable at $RH \geq 100\,\%$, being the Köhler theory more suitable to explain the compromise between the surface tension and solute concentration forces present in the wet aerosol particle. Lidar signal corresponds to the attenuated backscatter coefficient (β_{att}) derived from the PSD (see Figure 8 c). To determine β_{att}, β and AOD profiles are firstly derived through MOPSMAP (Gasteiger and Wiegner, 2018).

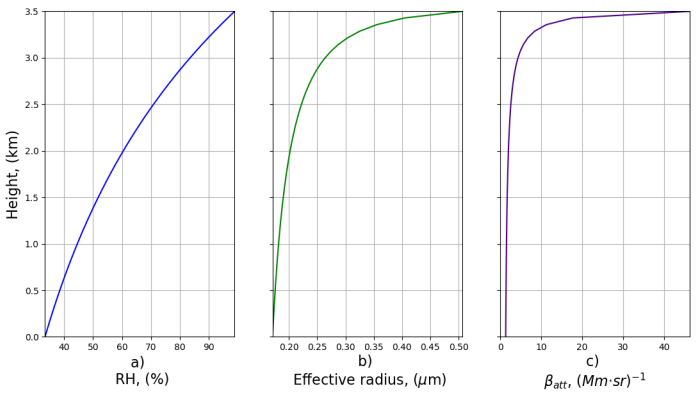

Figure 8. Relative humidity (RH), effective radius and attenuated backscatter coefficient (β_{att}) retrieved from the input parameters of Table 2

With the ascent of the saturated air parcel, the number of particles activated increases, and thus N_d. The DSD in this convective cloud formation is retrieved as follows: the largest PSD bin defines the minimum SS required to be activated as droplets. From this point, the SS is calculated in height according to the compromise of the height and the water-vapor 13 (see Figure 9 a). This process also considers the droplet condensation growth (see Figure 9 b), which varies depending on the temperature, the saturation mixing ratio, and the supersaturation present at each height, reducing the availability of water-vapor molecules.

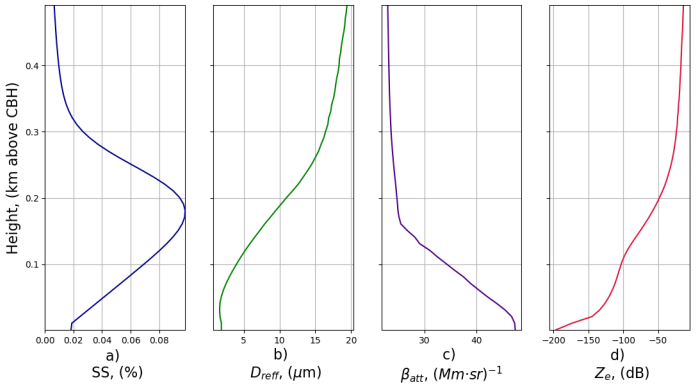

Figure 9. Supersaturation, droplet effective radius (D_{reff}), backscatter attenuated (β_{att}) and radar reflectivity factor (Z_e) retrieved from the input parameters of Table 2

Lidar and radar signals are derived once the PSD and DSD are obtained. The radar signal corresponds to the Z_e, which is directly derived from the DSD according to Pruppacher and Klett (1980) (see Figure 9 d). While lidar signal corresponds to the β_{att} produced by the PSD and DSD (see Figure 9 c).

To simulate the aerosol-cloud interaction, LARSS is launched with all the initial parameters present in Table 2 constant for different N_a, ranging between 5 to $20\,\#10^8/m^3$. Figure 10 shows the dependence between $log(N_a)$ and $log(N_D)$ for this case. The ACI_{Nd} index is the slope of $log(N_a) - log(N_D)$ line.

Atmospheric properties	Specie	Ammonium sulfate	Atmospheric conditions	Temperature $[T_o](K)$	298
	Number concentration $[N_a](\#10^8/m^3)$	5.0			
	Minimun radius (μm)	0.01		Pressure $[e_o](kPa)$	101
	Modal radius (μm)	0.1		Updraft $[w](m/s)$	2
	Maximun radius (μm)	0.5		Water-vapor ratio $[q_v]$	8
	Standard deviation $[\sigma]$	1.6	Instrumental parameters	Lidar wavelength (nm)	355
	Hygroscopicity parameter $[\kappa]$	0.51			
	Density (g/cm^3)	1.77		Radar wavelength (mm)	3.18
	Refrative index	$1.448+i7.49x10^{-6}$			

Table 2. Initial parameters used for the Case A_a Mészáros (1978); Hande et al. (2016); Curtis et al. (2007); Tu and Kanapilly (1978).

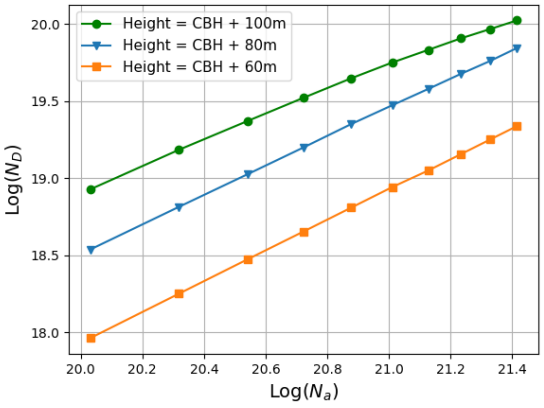

Figure 10. ACI index varying the initial number of aerosol for the accumulation mode ammonium sulfate using 10 iterations.

Similarly, according to Feingold et al. (2001), the ACI index (ACI_{reff}) can be estimated based on the D_{reff} as cloud proxy, keeping the β as an aerosol proxy. And, as aforementioned in Chapter 4.4, the ACI index (ACI_{Rs}) is obtained using Z_e as cloud proxy, and β as an aerosol proxy.

5.2. LARSS uncertainties

Input LARSS parameters vary in real atmospheric conditions, giving rise to uncertainties in the retrieved ACI index. The calculation of the ACI index error is complex due to the nonlinear physical phenomena related to aerosol particles (Pappalardo et al., 2004) and droplet formation. In similar cases, Monte Carlo technique (MCT) has been widely used in the literature to quantify uncertainties. MCT is based on the generation of random objects introduced 'artificially' or 'naturally' to solve purely deterministic problems. Those random objects are used to repeat the experiment enough times to obtain many quantities of interest using methods of statistical inference. Due to its statistical nature, its use has been extended in many research areas (Kroese et al., 2014). For example, Guerrero (2009) uses MCT to evaluate the uncertainty of aerosol-particle extinction coefficient profiles retrieved from lidar measurements, applying the Raman technique. In this work, MCT is implemented in LARSS (schematized in Figure 11) to determine the ACI index uncertainty as follows:

1. Table 2 shows the 13 initial parameters (P_1, P_2, ..., P_{13}). This set of parameters is noted as S.
2. The uncertainty associated to each parameter P is represented by its relative error ΔP.
3. A Gaussian distribution is associated to each parameter P where its standard deviation is defined by σ_P.
4. From each distribution, h random values are calculated (e.g., $P_{1,1}$, $P_{1,2}$, ..., $P_{1,h}$).
5. Random values are grouped in h sets (e.g., S_1,S_2, ..., S_h). For example, the set S_1 is given by $P_{1,1}$, $P_{2,1}$, ..., $P_{13,1}$.
6. h ACI indexes are retrieved with the generated sets.
7. The ACI index uncertainty is the standard deviation of the h ACI indexes.

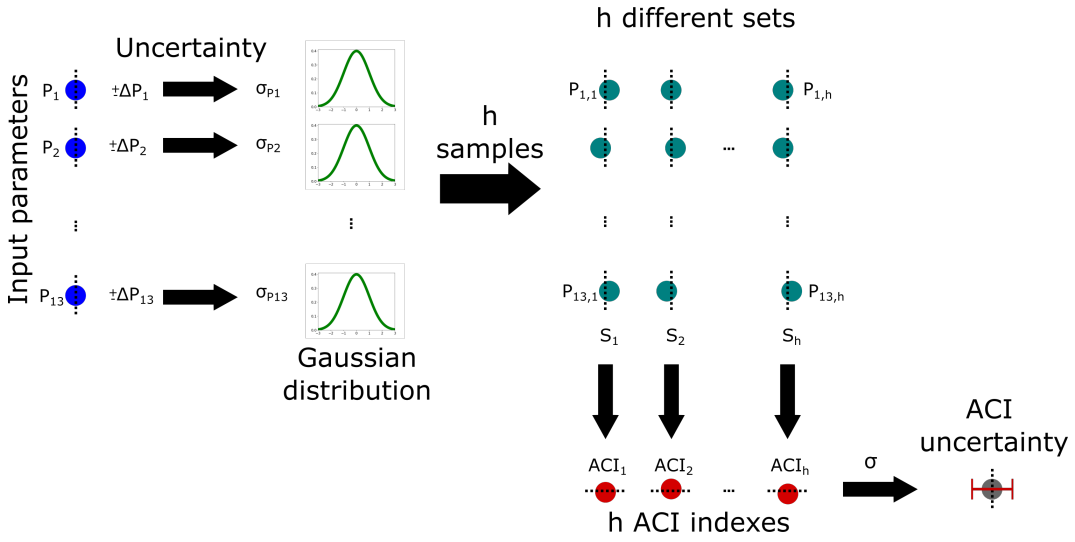

Figure 11. Monte Carlo thecnique scheme

Despite ACI index uncertainty depends on the number of simulations (h), it is expected that the ACI uncertainty converges once h is large enough. To identify the number of random values from which the ACI index uncertainty converges, the ACI uncertainty has been retrieved for several h ranging between 10 and 40 (being $\Delta P = 5\,\%$ for all the input parameters). Table 3 shows the convergence of the ACI uncertainty at $h = 30$.

h	ACI_{Rs} uncertainty	ACI_{reff} uncertainty	ACI_{Nd} uncertainty
10	0.05	0.020	0.07
20	0.04	0.016	0.05
30	0.03	0.011	0.04
40	0.03	0.014	0.05

Table 3. ACI uncertainty calculated by the Monte Carlo technique

Similarly, if the input parameters have an uncertainty of $\Delta P = 10\,\%$ the uncertainty for ACI_{Rs} is 0.05, for ACI_{reff} is 0.018, and for ACI_{Nd} is 0.06.

5.3. Notation of LARSS implemented cases

As LARSS simulation strongly depends on aerosol type and mode, simulated cases are named 'Case T_m' where T refers to the type: S=sulfate, B=biomass, D=dust and the subscript $_m$ refers to the mode: a=accumulation and c=coarse. For example, 'Case D_c' refers to a coarse-mode dust particle simulation. Aerosol mixture is noted as 'Case $T1_{m1}T2_{m2}$'. Accumulation mode aerosols have been mainly considered since are the most important mode for the natural formation of clouds. Fine mode aerosols require higher SS than those thought to exist in the free atmosphere to be activated, even for highly hygroscopic particles. Coarse mode aerosols require a lower SS to be activated, but they are much fewer in number concentration (Yau and Rogers, 1996).

Four monomodal cases are analyzed:

- Case A_a: Accumulation mode ammonium sulfate
- Case B_a: Accumulation mode burning biomass
- Case D_a: Accumulation mode dust
- Case D_c: Coarse-mode dust

Additionally, eleven aerosol-type mixtures have been simulated using the aforementioned four monomodal cases. It follows the most relevant mixtures:

- mixture of cases 1 and 3 (Case A_aD_a)
- mixture of cases 1, 2 and 4 (Case $A_aB_aD_c$)
- mixture of cases 1, 2, 3 and 4 (Case $A_aB_aD_aD_c$)

6. LARSS validation

To validate the LARSS performance, very well-known processes were simulated and the results were compared them with literature such as the dependence of the extinction-to-backscatter ratio of the dust with RH (Chapter 6.1), the evolution of the β_{att} in the vicinity of the CBH (Chapter 6.2), the dependence between SS_{cr} and D_{dry} for different aerosol types according to the Köhler theory (Chapter 6.3), the evolution of cloud properties with height (Sect. 6.4), and an example of Twomey effect (Sect. 6.4).

6.1. Optical properties: lidar ratio of dust

The extinction-to-backscatter ratio, also named lidar ratio, depends on the aerosol type (Ackermann, 1998; Giannakaki et al., 2010). However, it may also vary as a function of RH due to hygroscopic growth (Salemink et al., 1984). To validate the proper implementation of MOPSMAP in LARSS to simulate both aerosol optical properties and hygroscopic growth, the dependence of dust (Case $D_c D_a$) lidar ratio at 355 nm with RH is retrieved (see Figure 12). Lidar ratio at 355 nm ranges between 44 and 54 sr which is in agreement with a compilation of the lidar ratio of dust measured in different locations (values between 40 and 60 sr) (Shin et al., 2018). The lidar ratio trend, increasing with RH is also in agreement with Ackermann (1998), who reported a linear trend.

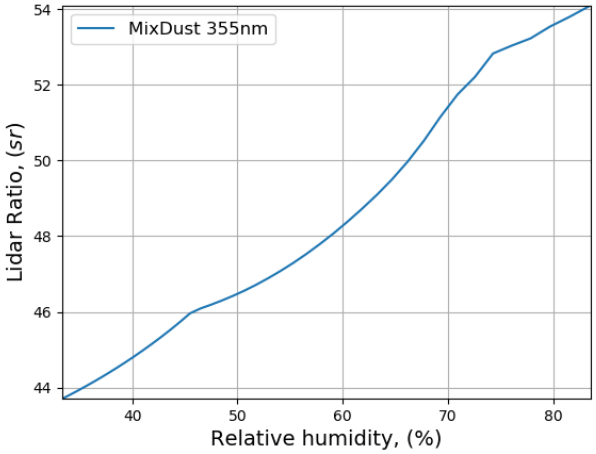

Figure 12. Dependence of the lidar ratio on the relative humidity for a mixture of dust.

Lidar ratio of clouds derived by LARRS varies between 17 and 22 sr, highlighting a larger scattering than absorption as expected. This range of values are quite similar to those presented by Comerón et al. (2017) in Barcelona (Spain) (from 16 to 26 sr) and by Ansmann et al. (1992) in Geesthacht (Germany) (from 13 to 23 sr).

The agreement of the LARSS-derived lidar ratio of dust and clouds with theoretical trends and experimental values found in the literature indicates a good performance of LARSS simulating droplet and aerosol-particle optical properties.

6.2. Lidar signature on the vicinity of the cloud base height

Figure 13 shows the β_{att} below and above the CBH (3.5 km asl) (blue and orange lines, respectively) simulated with Case A_a. β_{att} monotonically increases up to reach the CBH due to the hygroscopic growth of aerosol particles (blue line). Then, β_{att} strongly decreases due to the extinction increase above the CBH. This extinction is mainly caused by the scattering of droplets, which increase in size and number with height. Thus, β_{att} reaches the maximum peak at the very beginning of the cloud. These results are in agreement with the lidar and ceilometer signal shape under cloudy conditions (e.g., Jin et al., 2018). Indeed, this strong signature is

used for retrieving the CBH with lidar systems and ceilometers (e.g., Hey, 2014; Platt et al., 1994; Pal et al., 1992).

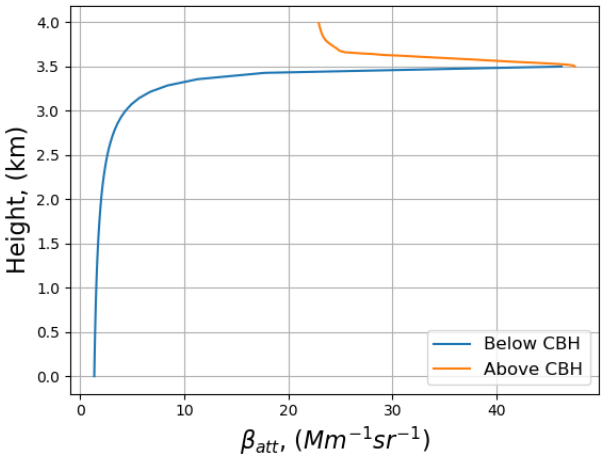

Figure 13. Backscatter attenuated (β_{att}) at $350nm$ signal retrieved from the PSD and DSD by the lidar.

6.3. Aerosol activation (Köhler theory)

Köhler theory describes the change in S due to a curved liquid-vapor interface, such as wet aerosol-particle surface (D'Almeida et al., 1991). This theory allows the calculation of the SS_{cr} from which the uptake of water-vapour molecules by particles of a given size (D_{cr}) becomes unstable (i.e., non-stop until SS disappears). In other words, an aerosol particle of diameter D_{cr} at SS_{cr} becomes a droplet. The SS_{cr} depends primarily on the D_{dry} and secondly in the hygroscopicity parameter (Dusek et al., 2006). According to Eq. 13, SS_{cr} increases with D_{dry} and decreases with the hygroscopicity parameter.

Figure 14 shows the SS_{cr} depending on D_{dry} for the aerosol types A_a, D_a and D_c simulated with LARSS. Regarding accumulation-mode types (i.e., A_a and D_a), it can be noted how aerosol type A_a requires less SS to be activated. This is because ammonia hygroscopicity parameter is greater than the dust one. Aerosols size also affects the SS_{cr}. The comparison between D_a and D_c (lines orange and red in Figure 14) shows that lower SS_{cr} activates large D_{dry}, independently of

hygroscopicity parameter. This behaviour has been widely studied (Junge and Mclaren, 1971; Dusek et al., 2006).

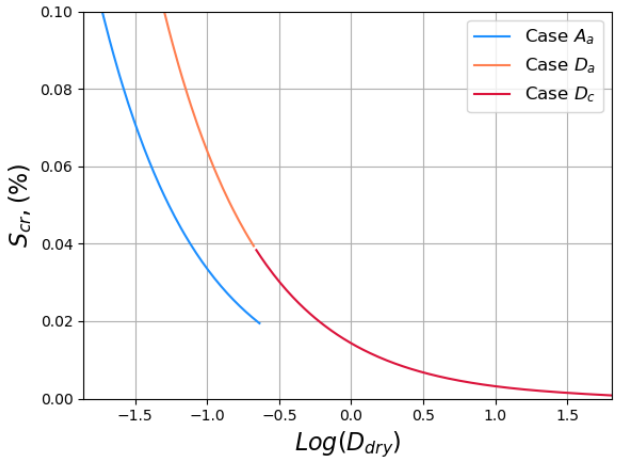

Figure 14. Critical supersaturation (S_{cr}) for accumulation mode ammonium sulfate, accumulation mode dust and coarse-mode dust.

6.4. Range-dependence of cloud microphysics

LARSS considers two processes within the cloud: droplet activation and condensation growth. Figure 15 shows the evolution with height of the most relevant cloud properties obtained with LARSS (such as SS, N_d, D_{reff}, σ, and LWP) for the aerosol type A_a. This figure can be successfully compared with Figure 7.4 of Yau and Rogers (1996) for sodium chloride. Despite the different aerosol types, the evolution of the cloud properties with height is in agreement. SS increases with height until reaching a SS_{max}. From this height, the amount of water vapor available decreases because the condensation of molecules due to droplet growth is larger than the increase of the μ_s caused by the cooling of the air mass. N_d increases with height, following the SS increases, until SS reaches SS_{max}, remaining constant from this height (Figure 15 b). The D_{reff} dependence with height can be separated into two regions. In the first region, the D_{reff} decreases because the activation of the lower radius is more important than the size increase due to the condensation growth of the droplets. In the second region ($\sim 85m$

above CBH), the number and size of droplets are larger enough so that the D_{reff} monotonically increases. The current version of LARSS does not consider the coalescence droplet growth, which starts at $D_{reff} = 20\mu m$. Figure 15 d) shows the variation of the standard deviation with height, increasing in the first heights due to the activation of new droplets until the height where SS_{max} is reached. The decrease of the DSD standard deviation with height is caused by the condensation growth (independent of the droplet size as mentioned in Sect. 3.3.1). Figure 15 c) and e) show that the D_{reff} and the liquid water content (LWC) increase non-linearly until maximum SS is reached, exhibiting almost a linear behavior from this point (heights $>$ CBH $+180m$). These results are in agreement with Brenguier (1991), Miles et al. (2000) and Pawlowska and Brenguier (2000) who have demonstrated that the D_{reff} and the LWC have a strong vertical structure in a well-mixed adiabatic atmosphere, increasing both almost linearly with the height from SS_{max}.

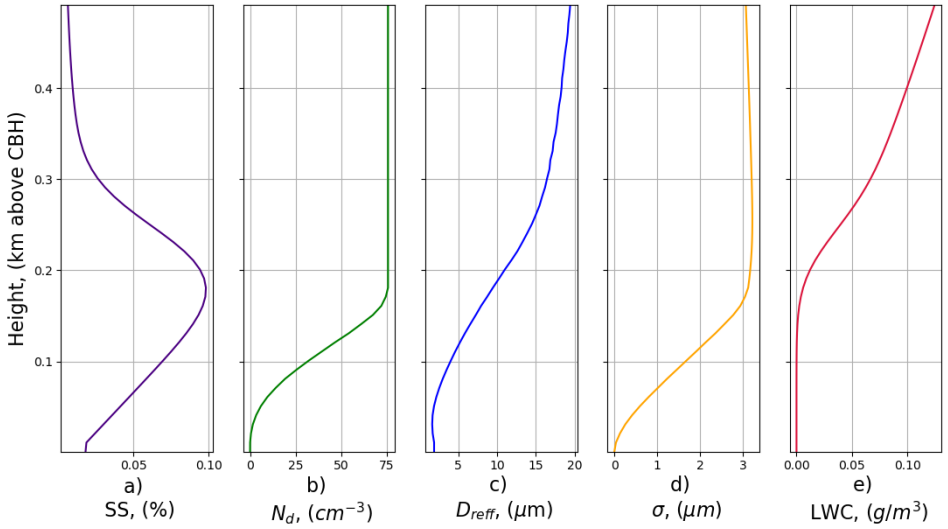

Figure 15. Early development of cloud properties: a) supersaturation (SS), b) droplet number concentration (N_d), c) droplet effective radius (D_{reff}), d) standard deviation (σ), e) liquid water content (LWC) in air ascending at constant velocity of $2m/s$.

6.5. Twomey effect

Twomey effect describes that an N_a increase results in a cloud albedo increase due to larger N_d and lower D_{reff} (Twomey, 1977). Feingold et al. (2003) evidence this effect for liquid-water clouds, single-layered, non-precipitating, and free of airborne insects using ground-based remote sensors. This cloud type has been simulated by LARSS for $N_a = 500\,\#/cm^3$ and $N_a = 2000\,\#/cm^3$, remaining the rest of input parameters constants. SS, N_d, D_{reff} and Z_e profiles of theses two cases are shown in Figure 16. As it can be seen, the increase of N_a causes a considerable increase of N_d from 76 to $189\,\#/cm^3$ at CBH+160 m (Figure 16b). The increase of N_d causes the decrease of available water-vapour molecules which explain the decrease of the SS_{max} from 0.1 at CBH+180m to 0.08 at CBH+140 m (Figure 16a). The effect of N_a in D_{reff} is negligible below CBH+200m (Figure 16c) and thus, Z_e at $N_a = 500\,\#/cm^3$ (green) is lower than at $N_a = 2000\,\#/cm^3$ (purple), following the N_d evolution. However, above CBH+250 m, the increase of D_{reff} at $N_a = 500\,\#/cm^3$ (green) is large enough that Z_e at $N_a = 500\,\#/cm^3$ (green) overcomes Z_e at $N_a = 2000\,\#/cm^3$ (purple). This Z_e dependence with the N_d and the D_{reff} can also be appreciated in Raghavan (2013b). It is worthy to note that the N_d (green curve) agrees with the N_d obtained by Mei et al. (2013) for ammonium sulfate at $SS = 0.12\,\%$.

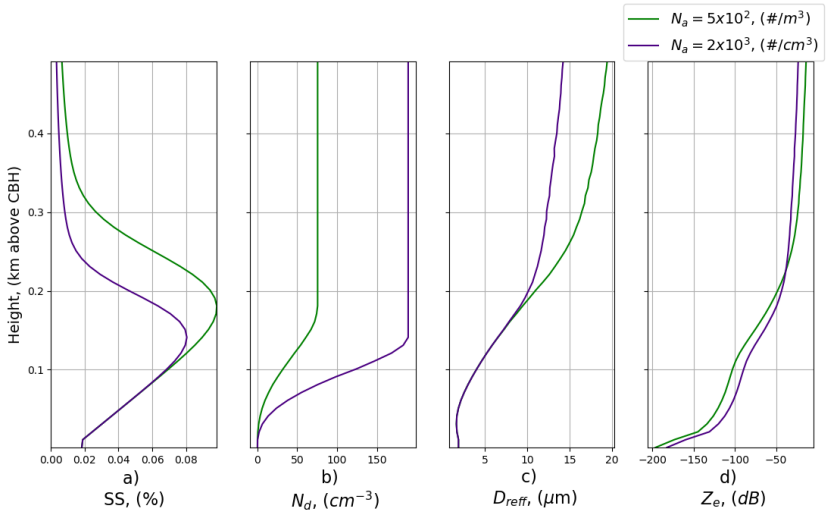

Figure 16. Twomey effect of a cloud formed from the activation of ammonium sulfate particles.

7. Results

In this section, the results obtained through the LARSS code are presented. Firstly, the calculation of the ACI index for monomodal distribution (Case A_a), it calculation for different mixtures of aerosol, and the influence of the presence of a coarse-mode in a bimodal distribution. Secondly, the study of the influence of variations in the aerosol dry and wet modal radius, and the updraft velocity. Finally, the relationship of the ACI_{Rs} and the ACI_{reff} as a function of the Angstrom exponent, and an intercomparison between the AF measured in Granada (Spain) and the calculated with LARSS.

7.1. Analysis of the ACI of ammonium sulfate

Figure 17 shows the ACI_{Nd} and ACI_{reff} evolution with height for the analyzed Case A_a (see input parameters in Table 2), and Z_e, where the red dashed line marks the height at which the minimum radar measurement value is reached [$-60dB$ (Sauvageot and Omar, 1987)]. ACI_{reff} increases with height, being negligible at the very beginning (near to the CBH) because only a few largest particles are activated and thus, Z_e is below the minimum radar sensitivity. ACI_{reff} reaches its maximum value from $350m$ above CBH ($LWP > 154g/m^2$). As it can be seen in Figure 17(left), ACI_{Nd} is equal to one at the very beginning, decreasing up to its minimum value (0.660 at CBH+180 m), where SS_{max} is reached. Thus, ACI_{Nd} minimum is reached at lower altitude (i.e., $170m$ below) than ACI_{reff} maximum.

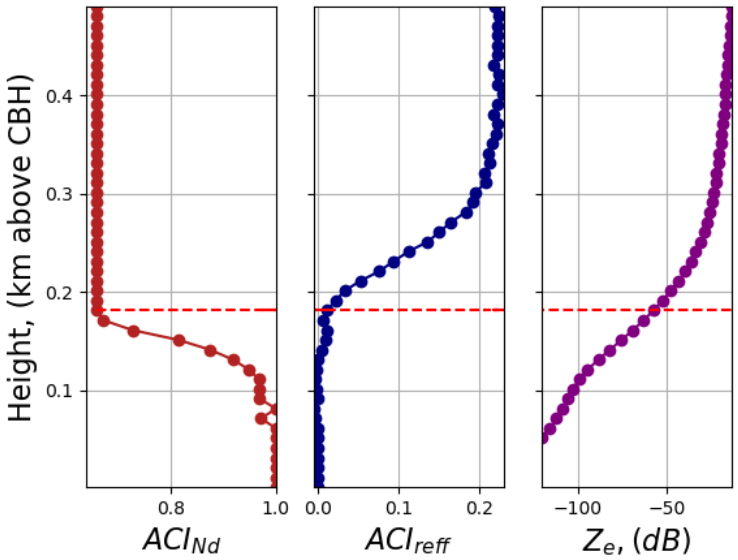

Figure 17. ACI_{Nd}, ACI_{reff} and radar reflectivity factor (Z_e) of ammonium sulfate, where the red dashed line marks the height at which the minimum radar sensitivity is reached.

7.2. ACI indexes of different aerosol types

In this section, LARSS simulations with aerosol types listed in Table 4 are used to analyze the ACI dependence on aerosol types. The hygroscopicity parameter, standard deviation and density of ammonium sulfate and dust are extracted from Hande et al. (2016). The hygroscopicity parameter and density of burning biomass are extracted from Psichoudaki et al. (2018) and Zhai et al. (2017), respectively. The minimum, modal, and maximun radius, and the N_a of the ammonium sulfate and dust are from Mészáros (1978) and Tu and Kanapilly (1978), and Dentener et al. (2006), respectively. The minimum, modal, and maximun radius, and the N_a of the burning biomass are from Remer et al. (1998) and Keil and Haywood (2003). The refractive index of ammonium sulfate, dust and burning biomass are extracted from Curtis et al. (2007), Denjean et al. (2016) and Remer et al. (1998), respectively. From Table 4, a total of 15 cases the ACI_{Nd} and ACI_{reff} has been analyzed (Figure 34) with the same atmospheric conditions, and the instrument parameters fixed according to the instrumentation available in the Granada station.

Atmospheric properties	Specie	Ammonium sulfate $[A_a]$	Burning Biomass $[B_a]$	Dust Accumulation $[D_a]$	Dust Coarse $[D_c]$	Atmospheric conditions	Temperature $[T_o](K)$	298
	Number concentration $[N_a](\#10^8/m^3)$	5.00	18.90	7.00	0.35			
	Minimun radius (μm)	0.01	0.05	0.05	0.50		Pressure $[e_o](kPa)$	101
	Modal radius (μm)	0.10	0.14	0.20	1.30		Updraft $[w](m/s)$	2
	Maximun radius (μm)	0.5	0.5	0.5	6.0		Water-vapor ratio $[q_v](g/kg)$	8
	Standard deviation $[\sigma]$	1.6	1.3	1.59	2.00	Instrumental parameters	Lidar wavelength (nm)	355
	Hygroscopicity parameter $[\kappa]$	0.51	0.22	0.14	0.14			
	Density (g/cm^3)	1.77	1.15	2.60	2.60		Radar wavelength (mm)	3.18
	Refrative index	$1.448+i7.49x10$	$1.520+i0.025$	$1.530+i0.008$	$1.530+i0.008$			

Table 4. Initial parameters used for the different aerosol types (Mészáros, 1978; Hande et al., 2016; Curtis et al., 2007; Tu and Kanapilly, 1978; D'Almeida et al., 1991; Dentener et al., 2006; Denjean et al., 2016; Keil and Haywood, 2003; Psichoudaki et al., 2018; Zhai et al., 2017; Li et al., 2016; Remer et al., 1998).

First, ACI_{Nd} and ACI_{reff} for different monomodal aerosol types are shown in Figure 18. The ACI indexes of accumulation-mode cases (A_a, B_a, and D_a) present similar behavior, increasing with height. ACI_{Nd} minima range between 0.447 and 0.718. No clear relationship between the N_a and the hygroscopicity parameter with the ACI indexes is found.

The case B_a presents negatives values in the ACI_{reff} from $CBH + 120$ to $CBH + 180m$ due to a positive relationship between N_a and the droplet effect radius. This phenomenon is called the anti-Twomey effect, and it has been evidenced in the Gulf of Mexico and South China Sea (Yuan et al., 2008). However, these results may be produced due to the low LWP present in this region (from 0.12 to $5.79 g/m^2$).

The case D_c is a special one because ACI_{Nd} and ACI_{reff} reaches the maximum theoretical value (1 and 0.33, respectively), i.e. the whole PSD is activated. This case would rarely occur in real atmospheric conditions since it requires the presence of pure coarse-mode dust PSD. The ACI indexes of case D_c also present a local minimum at $20m$, although, this behavior is not relevant since it would not be detectable by radar (i.e., region, where Z_e below the minimum radar sensitivity).

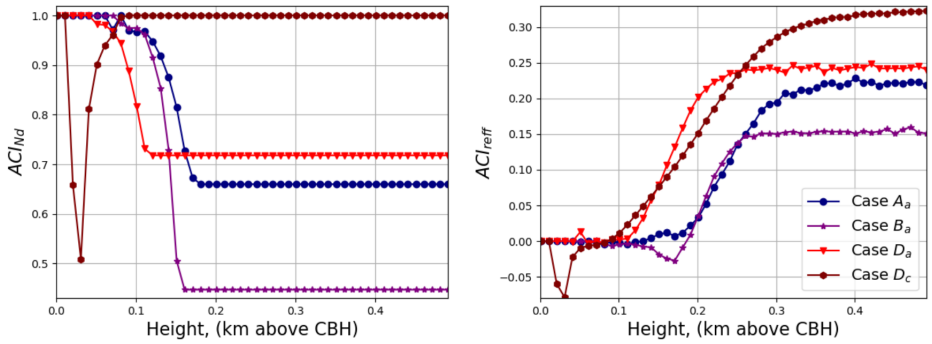

Figure 18. ACI_{Nd}, ACI_{reff} for different mixtures of two aerosol types according to the legend.

Figure 19 shows the ACI_{Nd} and ACI_{reff} for different two-type aerosol mixtures. For those mixtures without D_c, ACI index values depend on the predominance of the cloud condensation nuclei from the accumulation-mode (CCN_a) of each accumulation-mode type. Since D_a presents a higher N_a on the right side of the PSD, the N_d is always bigger than in other cases, making the ACI value of two-type mixtures closer to the ACI of type D_a if it is present.

In presence of D_c (case A_aD_c, case B_aD_c, and D_aD_c,) the ACI index is dominated by the coarse mode at the lowest altitudes, starting the activation of the accumulation mode from 60 to $80m$. This behavior is because D_c activation is reached at lower SS due to its bigger dry size (Dusek et al., 2006) (see Figure 14). Once the ACI_{Nd}/ACI_{reff} reaches its minimum/maximum, the value depends on the aerosol type of the accumulation mode. For case B_aD_c, $ACI_{Nd} = 0.659$ and $ACI_{reff} = 0.236$. The two-type mixture cases with D_c have ACI indexes similar to the monomodal Case D_c. This is because the coarse mode is completely activated (i.e., cloud condensation nuclei from coarse-mode [CCN_c]) whereas the accumulation mode (CCN_a) is only partially activated (i.e., CCN_a is lower than of CCN_c). The special case D_aD_c is analyzed in Section 7.2.1.

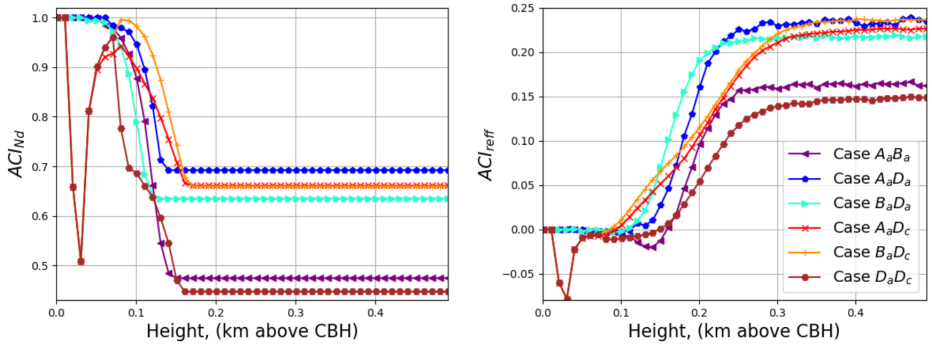

Figure 19. ACI_{Nd}, ACI_{reff} for different mixtures of three and four aerosol types according to the legend.

Figure 20 shows the ACI_{Nd} and ACI_{reff} for different mixtures of three and four aerosol types. In the same way to the mixtures of two aerosol types, the behavior below $CBH + 80m$ is equal to D_c in every case that contains it. The cases with D_aD_c present the lower ACI indexes since CCN_a is greater. Similarly, for the mixture of the four monomodal cases. Otherwise, the case $A_aB_aD_c$ presents larger ACI values, since CCN_a is almost equal to CCN_d. Finally, the case $A_aB_aD_a$ presents an ACI index closer to the accumulation mode dust and ammonium sulfate since its bigger the N_d of these modes.

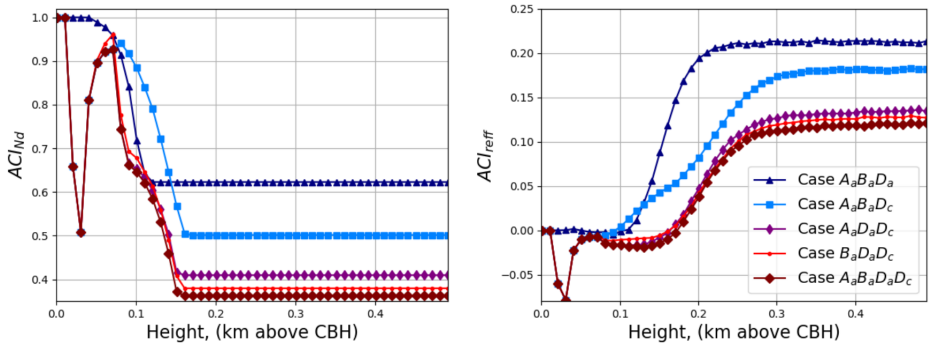

Figure 20. ACI_{Nd}, ACI_{reff} for different aerosol types according to the legend.

As it can be seen, ACI values are within the theoretical ranges ($0 < ACI_{Nd} < 1$ and $0 < ACI_{reff} < 0.33$) for heights above $CBH + 200m$ in all cases. Below this height, aerosol particle activation is not enough to be detected through ACI_{Nd}. It worthy to note that ACI_{reff} presents negatives values in the range CBH to CBH+200 meters.

This effect is due to the higher weight of the new droplets than the condensation growth in the D_{reff}.

7.2.1. Influence of the presence of a coarse mode

In Chapter 7.1, the ACI index was retrieved for a monomodal distribution of ammonia sulphate (type A_a). However, PSD used to be bimodal, e.g., D_aD_c. Figure 21 shows the influence on $ACI_{Nd-\beta}$ of the coarse-mode size, varying the coarse-mode N_a between 0 to $35e6\#/m^3$ with accumulation-mode N_a at $7e8\#/m^3$.

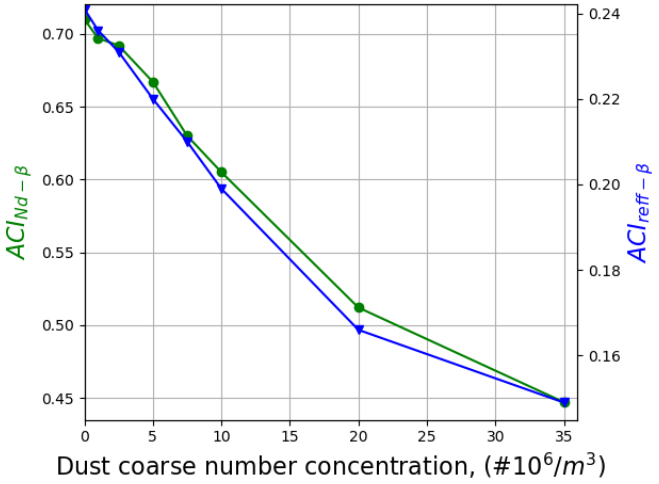

Figure 21. Accumulation mode dust ACI indexes variations due to the presence of a coarse mode.

The increases of the coarse-mode predominance causes an almost linear decrease of the $ACI_{Nd-\beta}$ (greater slope from 0 to $20\#10^6/m^3$) from the value of pure D_a of 0.718 to the mixture D_aD_c value of 0.447.

7.3. Sensitivity study of the ACI indexes to LARSS input parameters

Under real atmospheric conditions, updraft velocity, PSD and DSD varies with time, and thus, the lidar and radar signals. The present section shows the influence of

these changes on the ACI index for the Case A_a through the one-factor-at-a-time method. This method is similar to the Monte Carlo technique shown in Chapter 5.2, but varying only one parameter presented in Table 2.

7.3.1. Influence of the number of simulations in ACI indexes

The number of iterations (N) is the number of data points to derive the ACI index (see Figure 10). Thus, the decrease of N worsens the estimation of the ACI index. If no fluctuations are considered, N does not affect the ACI index value. However, if at least the fluctuation of one input parameter is considered, N becomes relevant. Figure 22 shows the relative error of ACI indexes (ΔACI) as a function of N using a dry modal radius fluctuations of $13\,\%$. As it can be seen, ΔACI reaches local minima at N equals to 20, 30, and 80. Due to the increase in the computational cost, N, it is fixed at 20. ΔACI is lower if AOD is used as aerosol proxy. β_{att} causes similar ΔACI (not shown). Considering that both proxies provide the same value of ACI, this result indicates that AOD is a better aerosol proxy to retrieve the ACI index.

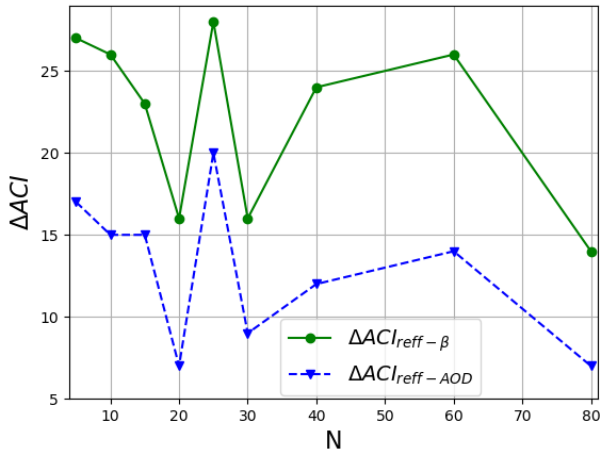

Figure 22. $\Delta ACI_{reff-\beta}$ and $\Delta ACI_{reff-AOD}$ with respect to the number of simulations (N).

7.3.2. Influence of the aerosol modal radius

The ACI experimental setup aims to measure changes in the cloud (i.e. N_d) due to changes in Na. However, random variations of the rest of the input parameter likely exist. The effect of changes of the dry aerosol-particle modal radius ($r_{m,dry}$) in $ACI_{reff-\beta}$ and $ACI_{reff-AOD}$ is studied in Figure 23. This figure shows the correlation coefficient of the linear fit to retrieve ACI indexes (R^2ACI), and the relative error between the ACI determined with a given $r_{m,dry}$ fluctuation, and the ACI determined without $r_{m,dry}$ fluctuations (ΔACI). While $r_{m,dry}$ fluctuations varies from 0 % to 97 %, R^2ACI decreases from ~ 0.99 to ~ 0 and ΔACI increases from 0 % to 99 %. According to these results, the $r_{m,dry}$ fluctuations must remain below 18 % during the experimental study to obtain a ΔACI below 30 % and R^2 greater than $0,76$. As aforementioned, the use of AOD as an aerosol proxy to retrieve the ACI index decreases the influence of the $r_{m,dry}$ fluctuations.

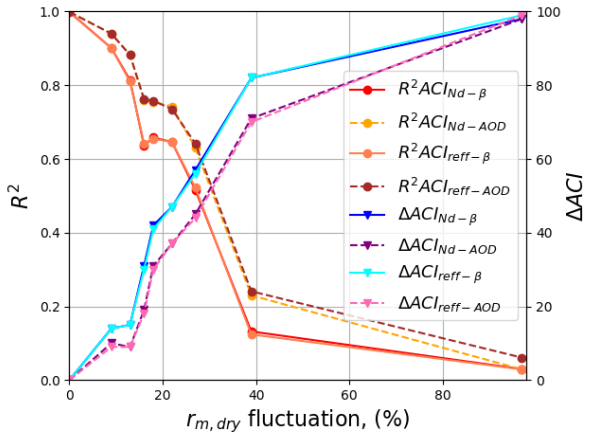

Figure 23. Correlation coefficients (R^2ACI) and relative errors (ΔACI) for $ACI_{Nd-\beta}$ and $ACI_{reff-\beta}$. For the sake of clarity, the ACI_{Rs} index is omitted in this figure and shown in Figure 31.

Since random variations may also occur in the vicinity of the CBH, the fluctuations of the wet aerosol-particle modal radius ($r_{m,wet}$) are also analyzed, obtaining trends similar to those shown in Figure 23 (see Figure 24). In this case, the $r_{m,wet}$ fluctuations must remain below $19\,\%$ to keep ΔACI below $21\,\%$ and R^2 greater than $0,80$. Thus, the fluctuations of $r_{m,dry}$ is more important than $r_{m,wet}$ in terms of ACI

accurate. This is an advantage of the experimental setup since it is easier to measure the $r_{m,dry}$ at the surface level than at the CBH. The influence of $r_{m,wet}$ on the rest of the ACI indexes, similar to $ACI_{Rs-\beta}$ and ACI_{Rs-AOD}, is shown in Figure 32.

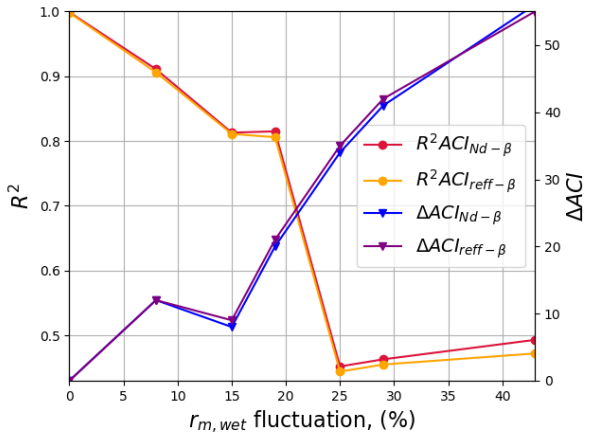

Figure 24. Correlation coefficients (R^2ACI) and relative errors (ΔACI) for $ACI_{Nd-\beta}$ and $ACI_{reff-\beta}$.

7.3.3. Influence of the updraft velocity

The sensitivity study of $ACI_{RS-\beta}$ with the updraft velocity (w) is based on Figure 25 where w fluctuation ranged from $0\,\%$ to $158\,\%$. Despite ΔACI remains very low even for large w uncertainties (e.g., $\Delta\text{ACI} = 25\,\%$ for $\Delta w = 119\,\%$). R^2ACI decreases considerably, affecting the ACI index reliability. According to these results, the w fluctuations must remain below $59\,\%$ during the experimental study to obtain a ΔACI below 9 % with a correlation of around 0.650. The influence of w on the rest of the ACI indexes, similar to $ACI_{Rs-\beta}$ and ACI_{Rs-AOD}, is shown in Figure 33.

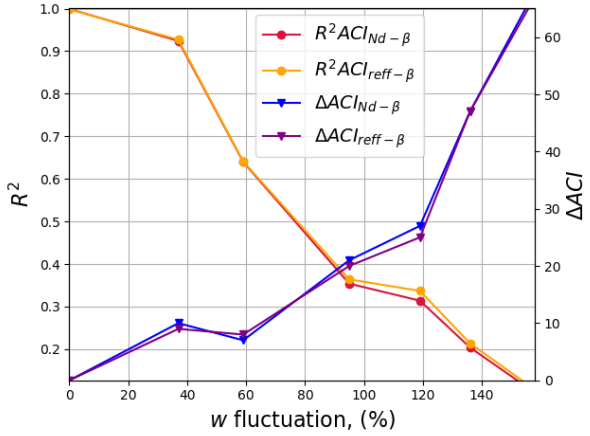

Figure 25. Correlation coefficients (R^2ACI) and relative errors (ΔACI) for $ACI_{Nd-\beta}$ and $ACI_{reff-\beta}$.

7.4. Proposal of ACI index based on Remote-sensing measurements

As aforementioned, D_{reff} and N_d properties can only be derived with algorithms that requires larges assumptions. To avoid intermediate steps that increases the uncertainty of the retrieved values, an ACI index directly based on Ze and β measurements (ACI_{Rs}) is proposed in this study (Sect. 4.4). Figure 26 shows the ACI_{Rs} for the aerosol type A_a which can be compared to the $ACI_{Nd-\beta}$ and $ACI_{reff-\beta}$ of Figure 17. As it can be seen, ACI_{Rs} presents the same trend than $ACI_{reff-\beta}$, but starting with negative values and increases with height till reaching a maximum value (0.664) above $CBH + 350m$.

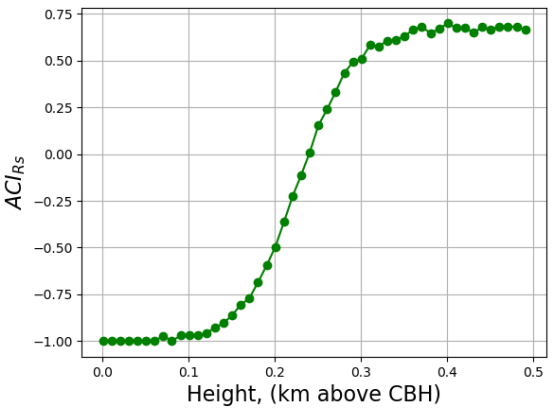

Figure 26. ACI_{Rs} of the Case A_a.

ACI_{Rs} has been retrieved for different mixtures of aerosol (see Figure 27 and 36), presenting a wider range ($[-1, 1]$) than the other ACI indexes. This amplitude is associated to the combined influence of N_d and D_{reff} in Z_e.

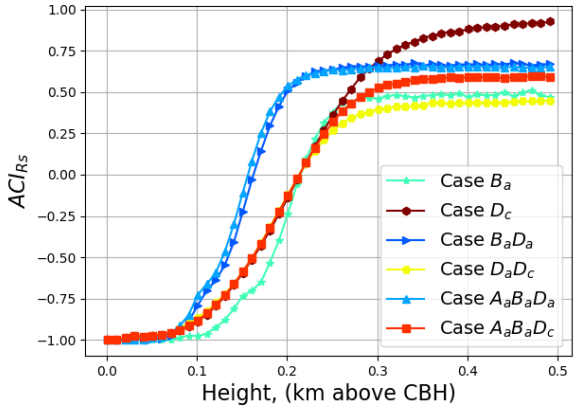

Figure 27. ACI_{Rs} for different cases according to the legend

Since there are no theoretical or experimental values of ACI_{Rs}, it is directly compared with ACI_{Nd} and ACI_{reff} in Figure 28. Despite ACI_{Nd} and ACI_{Rs} do not present any relationship, a high linear correlation between ACI_{reff} and ACI_{Rs} is found with $R^2 = 0.990$, improving up to $R^2 = 0.999$ restricting the linear fit to the region where Z_e is greater than -60 dB, (approximately the minimum radar sensitivity (Sauvageot and Omar, 1987)). Therefore, ACI_{reff} can be derived by means of the ACI_{Rs} as $ACI_{reff} = 0.161 \cdot ACI_{Rs} + 0.112$. However, this relationship depends on the aerosol type as shown in Figure 29 where ACI_{reff} and ACI_{Rs} are compared ($Z_e > -60dB$). It can be noticed that the aerosol type does not affect the slope (0.16) but the cut with the ordinate axis which varies from 0.117 (Case A_aD_a) to 0.072 (Case $A_aB_aD_a$). According to the backscatter-related Ansgtrom exponent (AE) shown in the label, trends can be grouped for $AE \geq 1.2$ (lines with blue color range) and ≤ 1.1 (lines with red color range), resulting in the mean ACI_{Rs}-to-ACI_{reff} conversion equations, $ACI_{reff} = 0.164 \cdot ACI_{Rs} + 0.112$ and $ACI_{reff} = 0.153 \cdot ACI_{Rs} + 0.073$, respectively. The uncertainty of this approximation is below 0.008 (a relative error of 4 % for A_a) which is a good approximation considering that this methodology avoids the need of

aerosol-particle and cloud microphysical inversion, which generates uncertainties over $45\,\%$ (Carslaw et al., 2013; Regayre et al., 2014; Change, 2007). The ACI_{Rs}-to-ACI_{reff} conversion cannot be applied for $AE \leq 0.6$ because small changes in the AE implies a large change in both the slope and the cut with the ordinate axis (see Figure 35).

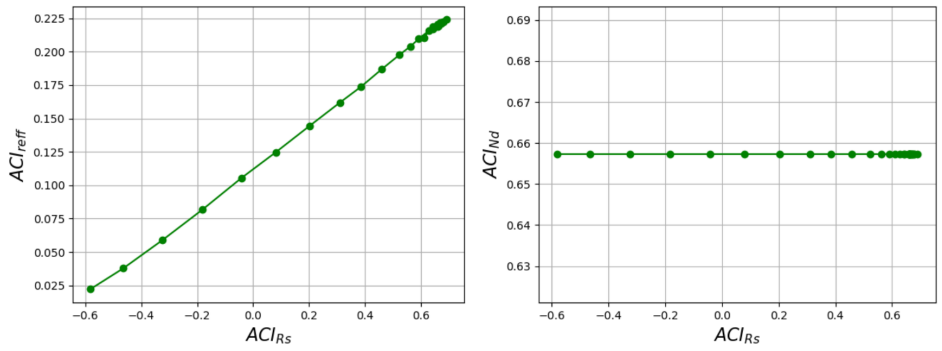

Figure 28. Relation between the ACI_{Nd} and ACI_{reff} with the ACI_{Rs} considering ACI values where Z_e greater than $-60dB$.

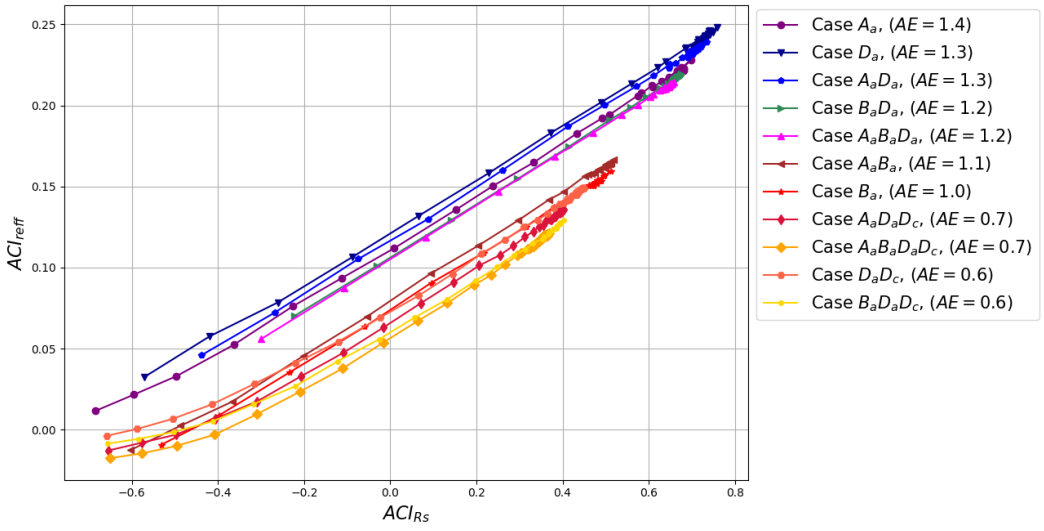

Figure 29. Relation between the ACI_{reff} with the ACI_{Rs} for different cases with AE from 1.4 to 0.6.

7.5. LARSS and in-situ activation fraction intercomparison

Table 5 shows the mean values of aerosol and droplet properties obtained at AGORA observatory (Andalusian Global Observatory of the Atmosphere). It includes two sampling sites: an urban background station located in the city of Granada (37.18^{o}N, 3.58^{o}W, 680 m a.s.l., UGR) and an alpine station located in Sierra Nevada mountain range (37.10^o N, 3.39^o W, 2500 m a.s.l., SNS). PSD and CCN concentration at UGR and SNS were measured by Rejano et al. (under review) for almost a whole year of measurements (from October of 2018 to May of 2019) at UGR and during the summer period (from June to August of 2019) at SNS. The activation factor (AF) was derived using the PSD and the CCN. The hygroscopicity parameter was derived from the particle chemical composition following a mixing rule as follows (Petters and Kreidenweis, 2007):

$$\kappa = \sum_i \epsilon_i \kappa_i \tag{26}$$

where ϵ_i and and κ_i are the volume fraction and the hygroscopic parameter of component i, respectively. Aerosol densities and chemical composition was obtained from 24-hour PM10 filter measurements during the same period. Five chemical species were identified (organic matter, inorganics, elemental carbon, sea salt, and mineral dust).

		UGR	SNS
Atmospheric aerosol properties	Number concentration $[N_d](\#10^8/m^3)$	130	27
	Minimun radius (μm)	0.012	0.012
	Modal radius $[D_{rmod}](\mu m)$	0.045	0.062
	Maximun radius (μm)	0.514	0.514
	Hygroscopicity parameter $[\kappa]$	0.186	0.198
	Density (g/cm^3)	1.76	2.08
	Refractive index	1.51 +0.005i	1.51 +0.005i
	Activation fraction $[AF]$	0.077	0.152
Cloud properties	CCN concentration $(\#10^8/m^3)$	10.06	4.13
	Supersaturation $[SS](\%)$	0.2	0.25

Table 5. Atmospheric and cloud parameter used as input parameters for LARSS model.

The mean and standard deviation of the AF at Granada (AF_{UGR}) and Sierra Nevada (AF_{SNS}) is compared with the AF derived from LARSS (AF_{LARSS}) using the atmospheric aerosol properties of Table 5 as input parameters. Figure 30 shows the evolution of the AF_{LARSS} with height until reaches the SS_{max} values of 0.20 ± 0.10 and 0.25 ± 0.10, respectively. These SS_{max} coincides with the SS at which AF_{UGR} and AF_{SNS} were obtained, allowing the intercomparison. Taking into account that AF_{LARSS} values are within the uncertainty range of the experimental AF, the simulated and experimental AF agrees. LARSS makes a subestimation of the AF with a relative difference of $25.2\,\%$ and $22.4\,\%$ for UGR and SNS, respectively. Agreeing with the relative difference between the predicted and measured CCN concentration of the results presented by Ervens et al. (2007) for $SS = 0.22$, and by Almeida et al. (2014) for $SS = 0.23$.

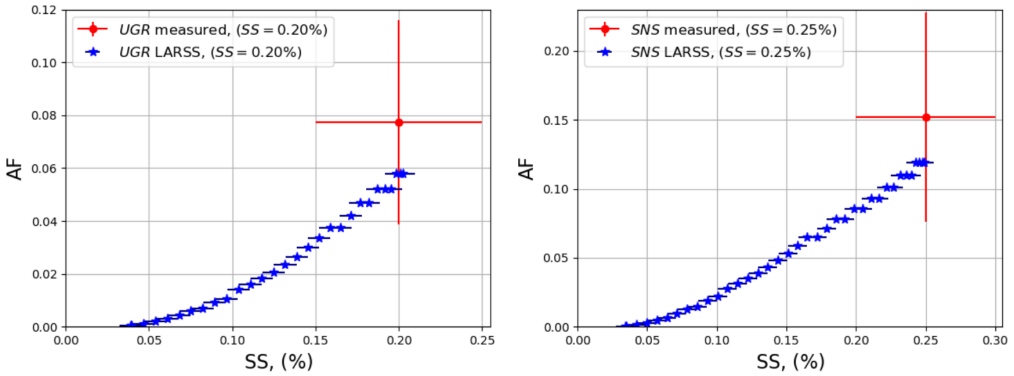

Figure 30. AF of the aerosol in Granada (UGR) and Sierra Nevada (SNS) for different maximum SS.

8. Conclusions

This study has presented the results of a lidar and radar signal simulator (LARSS) under convective cloud conditions for calculating the ACI index for different aerosol types. LARSS has been successfully validated through the simulation of well-known atmospheric processes. This tool has allowed investigating the optimal methodology to tackle the experimental-setup for observing the aerosol-cloud interaction (ACI) as well as its limitations.

This study has presented the results of a lidar and radar signal simulator (LARSS) under convective cloud conditions for investigating the optimal experimental-setup, as well as its limitations, to quantify the aerosol-cloud interaction (ACI). LARSS has been successfully validated through the simulation of well-known atmospheric processes. This tool has allowed calculating the ACI index for different aerosol types.

A literature review of the different effects of aerosols on clouds, such as its influence on the cloud albedo (first indirect effect) or the inhibition of clouds formation (semi-direct effect), was conducted. It is noted that the magnitude or direction of the effect of aerosols on clouds has not been clearly identified although several measurements and model simulations show the influence of aerosol on cloud formation and microphysics.

Lidar signal has been successfully retrieved from the particle size distribution (PSD) at each height. The aerosol hygroscopic growth in height has been calculated according to the Hänel theory up to $RH = 99$, while the cloud condensation nuclei (CCN) were obtained according to the Köhler theory from heights with $RH \geq 100$. Similarly, the radar signal has been retrieved from the droplet size distribution (DSD) at each height, where DSD changes in height due to the condensation growth.

ACI indexes have been retrieved based on aerosol-particle and cloud proxies such as aerosol-particle backscatter coefficient (β) and Aerosol Optical Depth

(AOD), and, cloud droplet concentration (N_d) and cloud droplet effective radius (D_{reff}), respectively. These measurements were calculated from several simulations, increasing the aerosol number concentration (N_a).

The aim of the simulated experimental setup is to quantify how N_a affects N_d and D_{reff}. However, to disentangle the aerosol particle effect on clouds, the rest of the variables shall be constant. Since real atmospheric conditions are rarely constant, the one-variable-at-a-time study has shown the influence of fluctuations in the input parameters (e.g., dry aerosol-particle modal radius $r_{m,dry}$, wet aerosol-particle modal radius $r_{m,wet}$, updraft velocity w). For example, $r_{m,dry}$ fluctuation must be below 18 % to obtain a ACI relative difference (ΔACI) below 30 %, which can be tracked with in-situ instrumentation (e.g., SMPS, APS) at ground level. Similarly, the Monte Carlo technique has been used to determine the ACI-index uncertainty caused by the uncertainty of the input parameters, e.g. temperature (T_o), hygroscopicity parameter (κ), standard deviation (σ). For the Case study A_a (ammonia sulfate) with an uncertainty of $5\,\%$ in all input parameters, ACI_{Nd}, ACI_{reff} and ACI_{Rs} presents a relative error of $6\,\%$, $5\,\%$, and $4\,\%$, respectively, were obtained. This indicates that ACI indexes can be observed through remote sensing instrumentation with a relatively low uncertainty despite the presence of fluctuations. However, if the fluctuations are too large, the effect of the aerosol in the clouds will be masked.

According to the once-variable-at-a-time study, AOD provides more accurate ACI indexes since both are similar, and the AOD is less affected than β to fluctuations of the input parameters (e.g., w and $r_{m,dry}$). This result joint to the fact that the Z_e dependence with D_{reff} is stronger than with N_d indicates that the optimal ACI index to be determined through remote sensing instrumentation (i.e., lidar and cloud radar) is $ACI_{reff-AOD}$. However, this ACI index requires the cloud microphysical inversion of Z_e measurements to derive the D_{reff}, using strong assumptions (e.g., DSD as log-normal size distribution). Thus, this study also provides a new methodology by which $ACI_{reff-AOD}$ is determined from a linear relationship with ACI_{Rs}, a new index that is determined with the direct

measurements AOD and Z_e (i.e., $ACI_{reff-AOD} = a \cdot ACI_{Rs} + b$) with $a = 0.164$ and $b = 0.112$ for $AE \geq 1.2$ and $a = 0.153$ and $b = 0.073$ for $AE < 1.2$. The ACI_{Rs}-to-ACI_{reff} conversion has an uncertainty below 0.008 (a relative error of 4 % for A_a), which is a good approximation considering that this methodology avoids the need for aerosol-particle and cloud microphysical inversion. This approximation is valid for $AE > 0.6$, i.e., in cases where the predominance of the coarse-mode is not too strong.

LARSS has also allowed studying the ACI indexes such as its evolution with height, showing that ACI_{Nd} (ACI_{reff}) decreases (increases) with height. ACI_{Nd} minimum value is reached at the SS_{max} height. However, the trend to the maximum (minimum) ACI index depends on the aerosol types. According to the 15 simulated cases, the ACI_{reff} reaches the maximum value above $CBH + 350m$, and thus, it can be concluded that the vicinity of the CBH shall be avoided to derive the ACI indexes.

The Activation Factor (AF) (i.e., CCN-to-N_a ratio) experimentally measured at the AGORA observatory in two sites (Granada and Sierra Nevada) has been simulated with LARSS. Results has pointed to a underestimation of the AF of 25 %, although the LARSS AF is within the uncertainty interval of the experimental one. Additionally, the relative difference is similar to the values presented by Ervens et al. (2007) for $SS = 0.22$, and by Almeida et al. (2014) for $SS = 0.23$.

Remote sensing instrumentation is a promising tool to investigate the aerosol-cloud interaction, although it has been highlighted that disentangling the aerosol effect on cloud microphysics in real atmospheric conditions might be challenging.

Despite the current version of LARSS allows a better understanding of the experimental approach of the aerosol influence in convective cloud formation, future developments including more processes, such as the coalescence droplet growth, may help to understand the aerosol-cloud interaction in other scenarios such as Stratocumulus clouds.

9. Abbreviations

The following abbreviations are used in this manuscript:

ACI	Aerosol-cloud interaction
AE	Angstrom exponent
AOD	Aerosol optical depth
CBH	Cloud base height
CCN	Cloud condensation nuclei
DSD	Droplet size distribution
LARSS	LidAr and Radar Signal Simulator
Lidar	Light Detection and Ranging or Laser Imaging Detection and Ranging
LWP	Liquid water path
MCT	Monte Carlo Technique
MOPSMAP	Modeled optical properties of ensembles of aerosol particles
PSD	Particle size distribution
Radar	Radio Detection And Ranging

Appendices

A. Additional figures

A.1. ACI_{Rs} sensitivity to $r_{m,dry}$, $r_{m,wet}$ and w.

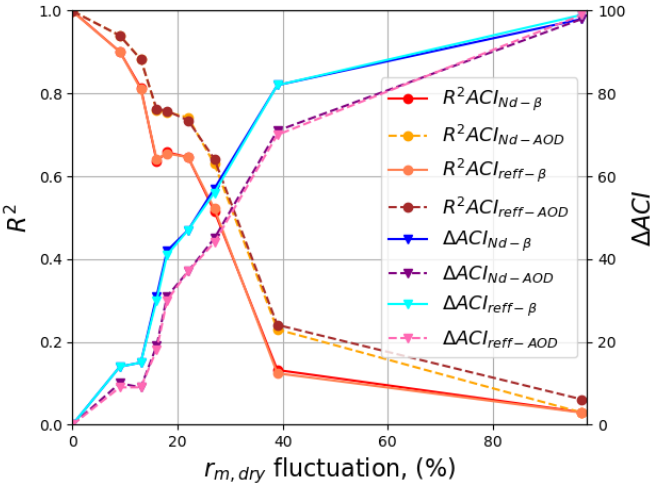

Figure 31. R^2 (left axis) and ΔACI (right axis) with respect to the $r_{m,dry}$ uncertainty.

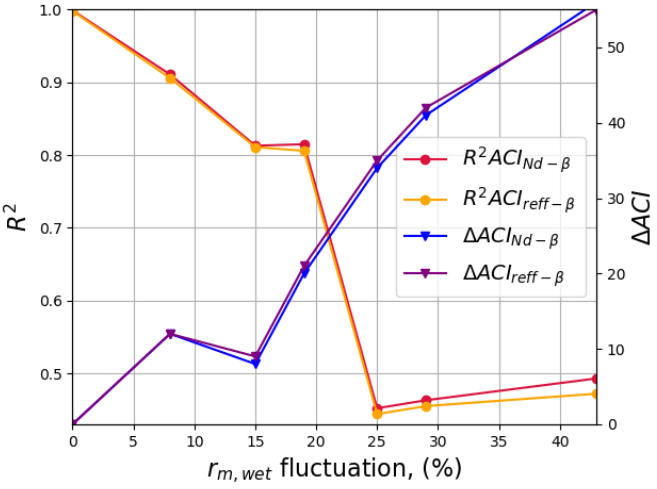

Figure 32. R^2 (left axis) and ΔACI (right axis) with respect to the $r_{m,wet}$ uncertainty. $R^2N_d - AOD$ and $\Delta ACIreff - AOD$ (not shown) are identical to $R^2N_d - \beta$ and $\Delta ACIreff - \beta$ because the uncertainty of $r_{m,wet}$ in the vecinity of the CBH does not affect the dry aerosol properties.

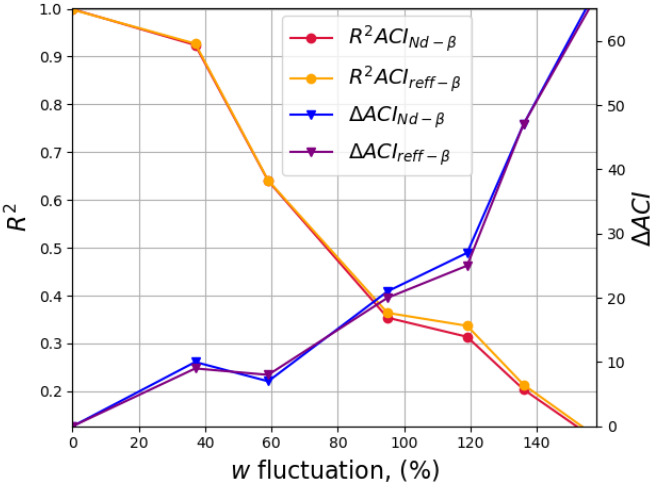

Figure 33. R^2 (left axis) and ΔACI (right axis) with respect to the w uncertainty. $R^2N_d - AOD$ and $\Delta ACIreff - AOD$ (not shown) are identical to $R^2N_d - \beta$ and $\Delta ACIreff - \beta$ because the uncertainty of w only affect within the cloud.

A.2. ACI_{Nd} and ACI_{reff} for all the cases used in LARSS

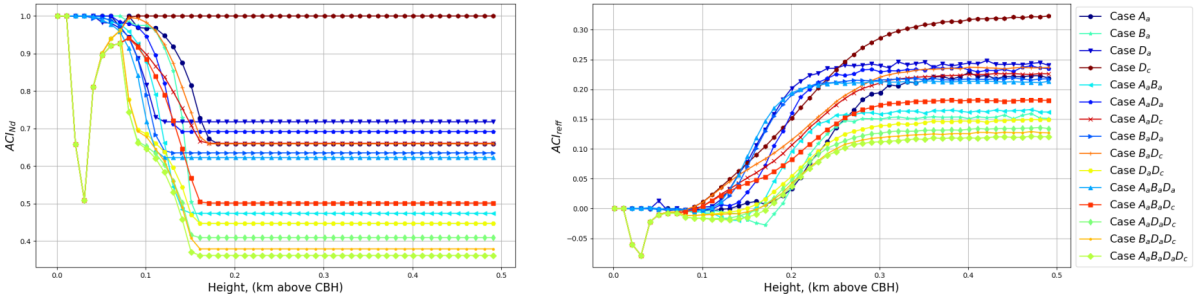

Figure 34. ACI_{Nd}, ACI_{reff} for different aerosol types according to the legend.

A.3. ACI_{Rs} to ACI_{reff} relation for all the cases used in LARSS

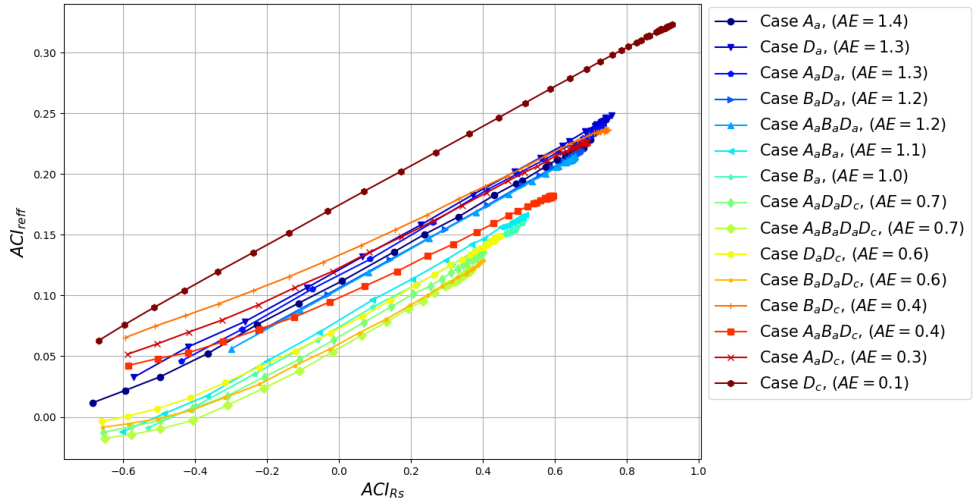

Figure 35. Relation between the ACI_{reff} with the ACI_{Rs} for different cases according to the legend.

A.4. ACI_{Rs} for all the cases used in LARSS

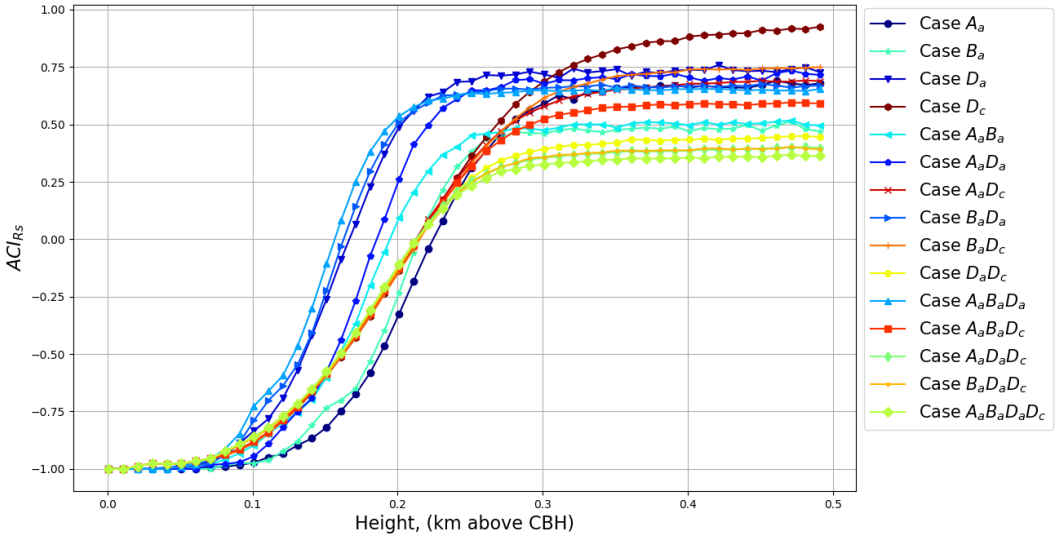

Figure 36. ACI_{Rs} for different cases according to the legend

B. List of symbols

Symbol	Description	Units
A	$3.3x10^{-5}/T$	m
A_1	$\frac{g}{RT}\left(\frac{L_w R}{c_p R_v T}-1\right)$	m^{-1}
A_2	$\frac{1}{q_v}+\frac{L_w^2}{c_p R_v T^2}$	-
A_{dry}	Aerosol dry diameter	μm
AF	Activation fraction	-
AOD	Aerosol optical depth	-
A_{wet}	Aerosol wet diameter	μm
B	$4.3m_s/M_s$	m^3
C	Initial supersaturation	-
CCN_a	Accumulation-mode cloud condensation nuclei	$\#/m^3$
CCN_c	Coarse-mode cloud condensation nuclei	$\#/m^3$
c_{pa}	Specific heat capacity of air	$J/kg\,K$
c_p	Specific heat capacity of most air at constant pressure	$J/kg\,K$
C_w	Coefficient of water vapor diffusion in the air	m^2/s
d	Wet diameter	μm
D_{cr}	Critical diameter	μm
D_d	Droplet diameter	μm
d_{dry}	Aerosol dry diameter	μm
D_{reff}	Droplet effective radius	μm
D_r	Droplet radius	μm
D_{r0}	Droplet initial radius	μm
D_{rmod}	Droplet modal radius	μm
e	Partial pressure of water vapor	Nm^{-2}
e_o	Reference Partial pressure of water vapor	Nm^{-2}
e_s	Saturation vapor pressure over plane water surface	Nm^{-2}
F_d	$\frac{\rho_w R_v T}{e_s(T) C_w}$	s/m^2
F_k	$\frac{\rho_w L_w^2}{k_a R_v T^2}$	s/m^2
F_x	$\frac{\rho_w L_w}{k_a T}$	s/m^2
g	Mean gravitational acceleration	m/s^2
q_v	water vapor mixing ratio (mass of water per 1 kg of air)	-
q_w	Liquid water mixing ratio (mass of liquid water per 1 kg of dry air)	-
k_a	Coefficient of air heat conductivity	$J/m\,s\,K$
$\lvert K_p\rvert$	$\left\lvert\frac{m_r-1}{m_r+2}\right\rvert^2$	$J/m\,s-$
L_w	Latent heat of water	J/kg
m	Real part of the refractive index	-
m_d	Mass of dry air	kg
m_r	Refractive index of water	-
m_s	Mass of the solute	kg
M_s	Average molar mass of atmospheric gases	kg/mol
M_w	Water molecular weight	kg/mol
m_v	Mass of water vapor	kg
$n_d(r,t)$	Droplet number concentration with a radius r	$\#/m^3$
N_a	Aerosol number concentration	$\#/m^3$
N_d	Droplet number concentration	$\#/m^3$
Q	$\frac{1}{F_d+F_k-F_x}$	m^2/s
R	Specific gas constant of most gases	$J/kg\,K$
R^2	Correlation coeficient	-
R_a	Specific gas constant of the dry air	$J/kg\,K$

Symbol	Description	Units
RH	Relative humidity	%
$r_{m,dry}$	Dry aerosol-particle modal radius	μm
$r_{m,wet}$	Wet aerosol-particle modal radius	μm
R_v	Specific gas constant of water vapor	$J/kg\,K$
S	Saturation ratio	-
SS	Supersaturation	-
SS_{cr}	Critical supersaturation	-
t	Time	s
T	Temperature	K
T_o	Reference temperature	K
w	Updraft velocity	m/s
z	Height from the reference height	m
z_c	Height from the cloud base	m
Z_e	Radar reflectivity	dB
z_o	Reference height	m
α_{ext}	extinction coefficient	m^{-1}
β	Backscatter coefficient	$1/Mm\,sr$
β_{att}	Attenuated backscatter coefficient	$1/Mm\,sr$
γ	Adiabatic temperature lapse rate	K/m
Γ_s	Saturation adiabatic temperature lapse rate	K/m
Δ ACI	Relative error of ACI	%
$\Delta r_{m,dry}$	Relative error of the dry aerosol-particle modal radius	%
$\Delta r_{m,wet}$	Relative error of the wet aerosol-particle modal radius	%
Δw	Relative error of the updraft velocity	%
κ	Hygroscopicity parameter	-
λ_r	Radar wavelength	mm
μ	Mixing ratio	g/kg
μ_s	Saturated mixing ratio	g/kg
ρ_a	Air density	kg/m^3
ρ_w	Water density	kg/m^3
σ	Standard deviation	-
$\sigma_{s/a}$	Surface tension of water	J/m^2
σ_b	Droplet effective cross-section	m^2

Bibliography

Ackerman, A. S., Toon, O., Stevens, D., Heymsfield, A., Ramanathan, V., and Welton, E. (2000). Reduction of tropical cloudiness by soot. Science, 288(5468):1042–1047.

Ackerman, A. S., Toon, O. B., and Hobbs, P. V. (1993). Dissipation of marine stratiform clouds and collapse of the marine boundary layer due to the depletion of cloud condensation nuclei by clouds. Science, 262(5131):226–229.

Ackermann, J. (1998). The extinction-to-backscatter ratio of tropospheric aerosol: A numerical study. Journal of atmospheric and oceanic technology, 15(4):1043–1050.

Albrecht, B. A. (1989). Aerosols, cloud microphysics, and fractional cloudiness. Science, 245(4923):1227–1230.

Almeida, G., Brito, J., Morales, C., Andrade, M., and Artaxo, P. (2014). Measured and modelled cloud condensation nuclei (ccn) concentration in são paulo, brazil: the importance of aerosol size-resolved chemical composition on ccn concentration prediction. Atmospheric Chemistry and Physics, 14:7559–7572.

Anderson, T. L., Charlson, R. J., Schwartz, S. E., Knutti, R., Boucher, O., Rodhe, H., and Heintzenberg, J. (2003). Climate forcing by aerosols–a hazy picture. Science, 300(5622):1103–1104.

Andreae, M. O., Rosenfeld, D., Artaxo, P., Costa, A., Frank, G., Longo, K., and Silva-Dias, M. d. (2004). Smoking rain clouds over the amazon. science, 303(5662):1337–1342.

Ansmann, A., Riebesell, M., Wandinger, U., Weitkamp, C., Voss, E., Lahmann, W., and Michaelis, W. (1992). Combined raman elastic-backscatter lidar for vertical profiling of moisture, aerosol extinction, backscatter, and lidar ratio. Applied Physics B, 55(1):18–28.

Boucher, O., Randall, D., Artaxo, P., Bretherton, C., Feingold, G., Forster, P., Kerminen, V.-M., Kondo, Y., Liao, H., Lohmann, U., et al. (2013). Clouds and aerosols. In Climate change 2013: the physical science basis. Contribution of Working Group I to the Fifth Assessment Report of the Intergovernmental Panel on Climate Change, pages 571–657. Cambridge University Press.

Brenguier, J.-L. (1991). Parameterization of the condensation process: A theoretical approach. Journal of the atmospheric sciences, 48(2):264–282.

Bréon, F.-M., Tanré, D., and Generoso, S. (2002). Aerosol effect on cloud droplet size monitored from satellite. Science, 295(5556):834–838.

Bringi, V. N. and Chandrasekar, V. (2001). Polarimetric Doppler weather radar: principles and applications. Cambridge university press.

Carslaw, K., Lee, L., Reddington, C., Pringle, K., Rap, A., Forster, P., Mann, G., Spracklen, D., Woodhouse, M., Regayre, L., et al. (2013). Large contribution of natural aerosols to uncertainty in indirect forcing. Nature, 503(7474):67–71.

Cavcar, M. (2000). The international standard atmosphere (isa). Anadolu University, Turkey, 30(9):1–6.

Change, I. P. O. C. (2007). Climate change 2007: The physical science basis. Agenda, 6(07):333.

Charlson, R. J., Schwartz, S., Hales, J., Cess, R. D., Coakley, J. J., Hansen, J., and Hofmann, D. (1992). Climate forcing by anthropogenic aerosols. Science, 255(5043):423–430.

Chin, M. and Kahn, R. (2009). Atmospheric aerosol properties and climate impacts, volume 2. US Climate Change Science Program.

Ciscar, J.-C., Soria, A., Goodess, C. M., Christensen, O. B., Iglesias, A., Garrote, L., Moneo, M., Quiroga, S., Feyen, L., Dankers, R., et al. (2009). Climate change impacts in europe. final report of the peseta research project. Technical report, Joint Research Centre (Seville site).

Comerón, A., Muñoz-Porcar, C., Rocadenbosch, F., Rodríguez-Gómez, A., and Sicard, M. (2017). Current research in lidar technology used for the remote sensing of atmospheric aerosols. Sensors, 17(6):1450.

Cook, J. and Highwood, E. (2004). Climate response to tropospheric absorbing aerosols in an intermediate general-circulation model. Quarterly Journal of the Royal Meteorological Society, 130(596):175–191.

Costantino, L. and Bréon, F.-M. (2010). Analysis of aerosol-cloud interaction from multi-sensor satellite observations. Geophysical Research Letters, 37(11).

Cotton, W. R. and Pielke Sr, R. A. (2007). Human impacts on weather and climate. Cambridge University Press.

Cui, Z., Carslaw, K. S., Yin, Y., and Davies, S. (2006). A numerical study of aerosol effects on the dynamics and microphysics of a deep convective cloud in a continental environment. Journal of Geophysical Research: Atmospheres, 111(D5).

Curtis, D. B., Aycibin, M., Young, M. A., Grassian, V. H., and Kleiber, P. D. (2007). Simultaneous measurement of light-scattering properties and particle size distribution for aerosols: Application to ammonium sulfate and quartz aerosol particles. Atmospheric Environment, 41(22):4748–4758.

D'Almeida, G. A., Koepke, P., and Shettle, E. P. (1991). Atmospheric aerosols: global climatology and radiative characteristics. A Deepak Pub.

Denjean, C., Cassola, F., Mazzino, A., Triquet, S., Chevaillier, S., Grand, N., Bourrianne, T., Momboisse, G., Sellegri, K., Schwarzenboeck, A., et al. (2016). Size distribution and optical properties of mineral dust aerosols transported in the western mediterranean. Atmospheric Chemistry and Physics, 16(2):1081–1104.

Dentener, F., Kinne, S., Bond, T., Boucher, O., Cofala, J., Generoso, S., Ginoux, P., Gong, S., Hoelzemann, J., Ito, A., et al. (2006). Emissions of primary aerosol and precursor gases in the years 2000 and 1750, prescribed data-sets for aerocom. Atmospheric Chemistry and Physics, 6(12):4321–4344.

Devasthale, A., Kruger, O., and Grassl, H. (2005). Change in cloud-top temperatures over europe. IEEE Geoscience and Remote Sensing Letters, 2(3):333–336.

Dusek, U., Frank, G., Hildebrandt, L., Curtius, J., Schneider, J., Walter, S., Chand, D., Drewnick, F., Hings, S., Jung, D., et al. (2006). Size matters more than chemistry for cloud-nucleating ability of aerosol particles. Science, 312(5778):1375–1378.

Ernst, W. G. and Ernst, W. G. (2000). Earth systems: processes and issues. Cambridge University Press.

Ervens, B., Cubison, M., Andrews, E., Feingold, G., Ogren, J. A., Jimenez, J. L., DeCarlo, P., and Nenes, A. (2007). Prediction of cloud condensation nucleus number concentration using measurements of aerosol size distributions and composition and light scattering enhancement due to humidity. Journal of Geophysical Research: Atmospheres, 112(D10S32).

Fan, J., Zhang, R., Li, G., Tao, W.-K., and Li, X. (2007). Simulations of cumulus clouds using a spectral microphysics cloud-resolving model. Journal of Geophysical Research: Atmospheres, 112(D4).

Fässler, A. (2019). Fast Track to Differential Equations. Springer.

Feingold, G., Eberhard, W. L., Veron, D. E., and Previdi, M. (2003). First measurements of the twomey indirect effect using ground-based remote sensors. Geophysical Research Letters, 30.

Feingold, G., Remer, L., Ramaprasad, J., and Kaufman, Y. (2001). Analysis of smoke impact on clouds in brazilian biomass burning regions: An extension of twomey's approach. Journal of Geophysical Research: Atmospheres, 106:22907–22922.

Fitzgerald, J. and Hoppel, W. (1984). Equilibrium size of atmospheric aerosol particles as a function of relative humidity: Calculations based on

measured aerosol properties. Journal of Geophysical Research: Atmospheres, 98(D4):7141–7147.

Fitzgerald, J. W., Hoppel, W. A., and Vietti, M. A. (1982). The size and scattering coefficient of urban aerosol particles at washington, dc as a function of relative humidity. Journal of the Atmospheric Sciences, 39(8):1838–1852.

Flossmann, A. I. and Wobrock, W. (2010). A review of our understanding of the aerosol–cloud interaction from the perspective of a bin resolved cloud scale modelling. Atmospheric Research, 97(4):478–497.

Gasteiger, J. and Wiegner, M. (2018). Mopsmap v1. 0: a versatile tool for the modeling of aerosol optical properties. Geoscientific Model Development, 11(7):2739–2762.

Giannakaki, E., Balis, D., Amiridis, V., and Zerefos, C. (2010). Optical properties of different aerosol types: seven years of combined raman-elastic backscatter lidar measurements in thessaloniki, greece. Atmospheric measurement techniques, 3(3):569.

Goren, T. and Rosenfeld, D. (2012). Satellite observations of ship emission induced transitions from broken to closed cell marine stratocumulus over large areas. Journal of Geophysical Research: Atmospheres, 117(D17).

Guerrero, J. L. (2009). Técnica lidar para la caracterización atmosférica mediante dispersión elástica y ramán. PhD thesis, Centro andaluz del medio ambiente, Universidad de Granada. Granada.

Hande, L. B., Engler, C., Hoose, C., and Tegen, I. (2016). Parameterizing cloud condensation nuclei concentrations during hope. Atmospheric Chemistry and Physics, 16(18):12059–12079.

Hänel, G. (1976). The properties of atmospheric aerosol particles as functions of the relative humidity at thermodynamic equilibrium with the surrounding moist air. In Advances in geophysics, volume 19, pages 73–188. Elsevier.

Hey, J. D. V. (2014). A novel LIDAR ceilometer: Design, implementation and characterisation. Springer.

Hobbs, P. V. (1993). Aerosol-cloud-climate interactions. Academic Press.

Jia, H., Ma, X., and Liu, Y. (2019). Exploring aerosol–cloud interaction using vocals-rex aircraft measurements. Atmospheric Chemistry and Physics, 19(12):7955–7971.

Jillavenkatesa, A., Dapkunas, S. J., and Lum, L.-S. H. (2001). Particle size characterization, volume 960. National Institute of Standards and Technology.

Jin, M. and Shepherd, J. M. (2008). Aerosol relationships to warm season clouds and rainfall at monthly scales over east china: Urban land versus ocean. Journal of Geophysical Research: Atmospheres, 113(D24).

Jin, Y., Sugimoto, N., Shimizu, A., Nishizawa, T., Kai, K., Kawai, K., Yamazaki, A., Sakurai, M., and Wille, H. (2018). Evaluation of ceilometer attenuated backscattering coefficients for aerosol profile measurement. Journal of Applied Remote Sensing, 12(4):042604.

Johnson, B., Shine, K., and Forster, P. (2004). The semi-direct aerosol effect: Impact of absorbing aerosols on marine stratocumulus. Quarterly Journal of the Royal Meteorological Society, 130(599):1407–1422.

Junge, C. and Mclaren, E. (1971). Relationship of cloud nuclei spectra to aerosol size distribution and composition. Journal of the atmospheric sciences, 28(3):382–390.

Kalivitis, N., Kerminen, V.-M., Kouvarakis, G., Stavroulas, I., Bougiatioti, A., Nenes, A., Manninen, H., Petäjä, T., Kulmala, M., Mihalopoulos, N., et al. (2015). Atmospheric new particle formation as a source of ccn in the eastern mediterranean marine boundary layer. Atmospheric Chemistry and Physics, 15:11143–11178.

Kaufman, Y. J. and Fraser, R. S. (1997). The effect of smoke particles on clouds and climate forcing. Science, 277(5332):1636–1639.

Kaufman, Y. J. and Koren, I. (2006). Smoke and pollution aerosol effect on cloud cover. Science, 313(5787):655–658.

Kaufman, Y. J., Koren, I., Remer, L. A., Rosenfeld, D., and Rudich, Y. (2005). The effect of smoke, dust, and pollution aerosol on shallow cloud development over the atlantic ocean. Proceedings of the National Academy of Sciences, 102(32):11207–11212.

Keil, A. and Haywood, J. M. (2003). Solar radiative forcing by biomass burning aerosol particles during safari 2000: A case study based on measured aerosol and cloud properties. Journal of Geophysical Research: Atmospheres, 108(D13).

Khain, A., Pokrovsky, A., and Sednev, I. (1999). Some effects of cloud–aerosol interaction on cloud microphysics structure and precipitation formation: Numerical experiments with a spectral microphysics cloud ensemble model. Atmospheric research, 52(3):195–220.

Khain, A., Rosenfeld, D., and Pokrovsky, A. (2005). Aerosol impact on the dynamics and microphysics of deep convective clouds. Quarterly Journal of the Royal Meteorological Society: A journal of the atmospheric sciences, applied meteorology and physical oceanography, 131(611):2639–2663.

Klett, J. D. (1981). Stable analytical inversion solution for processing lidar returns. Applied optics, 20(2):211–220.

Köhler, H. (1936). The nucleus in and the growth of hygroscopic droplets. Transactions of the Faraday Society, 32:1152–1161.

Koren, I., Kaufman, Y. J., Rosenfeld, D., Remer, L. A., and Rudich, Y. (2005). Aerosol invigoration and restructuring of atlantic convective clouds. Geophysical Research Letters, 32(14).

Koutsoyiannis, D. (2012). Clausius–clapeyron equation and saturation vapour pressure: simple theory reconciled with practice. European Journal of physics, 33(2):295.

Kovalev, V. A. and Eichinger, W. E. (2004). Elastic lidar: theory, practice, and analysis methods. John Wiley & Sons.

Kroese, D. P., Brereton, T., Taimre, T., and Botev, Z. I. (2014). Why the monte carlo method is so important today. Wiley Interdisciplinary Reviews: Computational Statistics, 6(6):386–392.

Levin, Z. and Cotton, W. R. (2008). Aerosol pollution impact on precipitation: a scientific review. Springer Science & Business Media.

Li, C., Hu, Y., Chen, J., Ma, Z., Ye, X., Yang, X., Wang, L., Wang, X., and Mellouki, A. (2016). Physiochemical properties of carbonaceous aerosol from agricultural residue burning: Density, volatility, and hygroscopicity. Atmospheric Environment, 140:94–105.

Li, G., Zhang, R., Fan, J., and Tie, X. (2007). Impacts of biogenic emissions on photochemical ozone production in houston, texas. Journal of Geophysical Research: Atmospheres, 112(D10).

Lihavainen, H., Kerminen, V.-M., and Remer, L. (2010). Aerosol-cloud interaction determined by both in situ and satellite data over a northern high-latitude site. Atmospheric Chemistry and Physics, 10(22):10987–10995.

Liu, Y. and Daum, P. H. (2002). Indirect warming effect from dispersion forcing. Nature, 419(6907):580–581.

Mei, F., Setyan, A., Zhang, Q., and Wang, J. (2013). Ccn activity of organic aerosols observed downwind of urban emissions during cares. Atmos. Chem. Phys, 13(24):12–155.

Mészáros, A. (1978). On the concentration and size distribution of atmospheric sulfate particles under rural conditions. Atmospheric Environment (1967), 12(12):2425–2428.

Miles, N. L., Verlinde, J., and Clothiaux, E. E. (2000). Cloud droplet size distributions in low-level stratiform clouds. Journal of the atmospheric sciences, 57(2):295–311.

Myhre, G., Stordal, F., M, J., Kaufman, Y., Rosenfeld, D., Storelvmo, T., Kristjánsson, J., Berntsen, T., A, M., and Isaksen, I. (2007). Aerosol-cloud interaction inferred from modis satellite data and global aerosol models. ATMOSPHERIC CHEMISTRY AND PHYSICS.

North, G. R., Pyle, J. A., and Zhang, F. (2014). Encyclopedia of atmospheric sciences, volume 1. Elsevier.

Padmakumari, B., Maheskumar, R., Harikishan, G., Morwal, S., Prabha, T., and Kulkarni, J. (2013). In situ measurements of aerosol vertical and spatial distributions over continental india during the major drought year 2009. Atmospheric Environment, 80:107–121.

Pal, S. R., Steinbrecht, W., and Carswell, A. I. (1992). Automated method for lidar determination of cloud-base height and vertical extent. Applied optics, 31(10):1488–1494.

Pappalardo, G., Amodeo, A., Pandolfi, M., Wandinger, U., Ansmann, A., Bösenberg, J., Matthias, V., Amiridis, V., De Tomasi, F., Frioud, M., et al. (2004). Aerosol lidar intercomparison in the framework of the earlinet project. 3. raman lidar algorithm for aerosol extinction, backscatter, and lidar ratio. Applied optics, 43(28):5370–5385.

Pawlowska, H. and Brenguier, J.-L. (2000). Microphysical properties of stratocumulus clouds during ace-2. Tellus B, 52(2):868–887.

Pawlowska, H., Grabowski, W. W., and Brenguier, J.-L. (2006). Observations of the width of cloud droplet spectra in stratocumulus. Geophysical research letters, 33(19).

Penner, J. E., Andreae, M., Annegarn, H., Barrie, L., Feichter, J., Hegg, D., Jayaraman, A., Leaitch, R., Murphy, D., Nganga, J., et al. (2001). Aerosols, their direct and indirect effects. In Climate Change 2001: The Scientific Basis. Contribution of Working Group I to the Third Assessment Report of the Intergovernmental Panel on Climate Change, pages 289–348. Cambridge University Press.

Penner, J. E., Zhang, S. Y., and Chuang, C. C. (2003). Soot and smoke aerosol may not warm climate. Journal of Geophysical Research: Atmospheres, 108(D21).

Petters, M. and Kreidenweis, S. (2007). A single parameter representation of hygroscopic growth and cloud condensation nucleus activity. Atmospheric Chemistry and Physics, 7(8):1961–1971.

Pinsky, M., Mazin, I., Korolev, A., and Khain, A. (2014). Supersaturation and diffusional droplet growth in liquid clouds: Polydisperse spectra. Journal of Geophysical Research: Atmospheres, 119(22):12–872.

Platt, C., Young, S., Carswell, A., Pal, S., McCormick, M., Winker, D., DelGuasta, M., Stefanutti, L., Eberhard, W., Hardesty, M., et al. (1994). The experimental cloud lidar pilot study (eclips) for cloud–radiation research. Bulletin of the American Meteorological Society, 75(9):1635–1654.

Pruppacher, H. R. and Klett, J. D. (1980). Microphysics of clouds and precipitation. Nature, 284(5751):88–88.

Psichoudaki, M., Nenes, A., Florou, K., Kaltsonoudis, C., and Pandis, S. N. (2018). Hygroscopic properties of atmospheric particles emitted during wintertime biomass burning episodes in athens. Atmospheric Environment, 178:66–72.

Radke, L. F., Coakley, J. A., and King, M. D. (1989). Direct and remote sensing observations of the effects of ships on clouds. Science, 246(4934):1146–1149.

Raghavan, S. (2013a). Radar meteorology, volume 27. Springer Science & Business Media.

Raghavan, S. (2013b). Radar meteorology, volume 27. Springer Science & Business Media.

Ramachandran, S. (2018). Atmospheric aerosols: Characteristics and radiative effects. CRC Press.

Regayre, L., Pringle, K., Booth, B., Lee, L., Mann, G., Browse, J., Woodhouse, M., Rap, A., Reddington, C., and Carslaw, K. (2014). Uncertainty in the magnitude

of aerosol-cloud radiative forcing over recent decades. Geophysical Research Letters, 41(24):9040–9049.

Remer, L., Kaufman, Y., Holben, B., Thompson, A., and McNamara, D. (1998). Biomass burning aerosol size distribution and modeled optical properties. Journal of Geophysical Research: Atmospheres, 103(D24):31879–31891.

Rosenfeld, D. (1999). Trmm observed first direct evidence of smoke from forest fires inhibiting rainfall. Geophysical research letters, 26(20):3105–3108.

Rosenfeld, D. (2000). Suppression of rain and snow by urban and industrial air pollution. Science, 287(5459):1793–1796.

Rosenfeld, D., Kaufman, Y. J., and Koren, I. (2006). Switching cloud cover and dynamical regimes from open to closed benard cells in response to the suppression of precipitation by aerosols. Atmospheric Chemistry and Physics, 6(9):2503–2511.

Rosenfeld, D., Sherwood, S., Wood, R., and Donner, L. (2014). Climate effects of aerosol-cloud interactions. Science, 343(6169):379–380.

Salemink, H., Schotanus, P., and Bergwerff, J. (1984). Quantitative lidar at 532 nm for vertical extinction profiles and the effect of relative humidity. Applied Physics B, 34(4):187–189.

Sarna, K. and Russchenberg, H. W. (2016). Ground-based remote sensing scheme for monitoring aerosol–cloud interactions. Atmospheric Measurement Techniques (Online), 9(3):1039–1050.

Sauvageot, H. and Omar, J. (1987). Radar reflectivity of cumulus clouds. Journal of Atmospheric and Oceanic Technology, 4(2):264–272.

Shin, S.-K., Tesche, M., Kim, K., Kezoudi, M., Tatarov, B., Müller, D., and Noh, Y. (2018). On the spectral depolarisation and lidar ratio of mineral dust provided in the aeronet version 3 inversion product. Atmospheric Chemistry and Physics, 18(17):12735–12746.

Solomon, S., Qin, D., Manning, M., Alley, R. B., Berntsen, T., Bindoff, N. L., Chen, Z., Chidthaisong, A., Gregory, J. M., Hegerl, G. C., et al. (2007). Technical summary. Cambridge University Press, 151.

Stocker, T. F., Qin, D., Plattner, G.-K., Tignor, M. M., Allen, S. K., Boschung, J., Nauels, A., Xia, Y., Bex, V., and Midgley, P. M. (2014). Climate change 2013: The physical science basis. contribution of working group i to the fifth assessment report of ipcc the intergovernmental panel on climate change.

Sullivan, R., Moore, M., Petters, M., Kreidenweis, S., Roberts, G., and Prather, K. (2009). Effect of chemical mixing state on the hygroscopicity and cloud nucleation properties of calcium mineral dust particles. Atmospheric Chemistry & Physics, 9(10):3303–3316.

Teller, A. and Levin, Z. (2006). The effects of aerosols on precipitation and dimensions of subtropical clouds: a sensitivity study using a numerical cloud model. Atmospheric Chemistry and Physics, 6(1):67–80.

Tu, K. and Kanapilly, G. (1978). Generation and characterization of submicron ammonium sulfate and ammonium hydrogen sulfate aerosols. Atmospheric Environment (1967), 12(8):1623–1629.

Twomey, S. (1977). The influence of pollution on the shortwave albedo of clouds. Journal of the atmospheric sciences, 34(7):1149–1152.

Twomey, S. and Wojciechowski, T. (1969). Observations of the geographical variation of cloud nuclei. Journal of the Atmospheric Sciences, 26(4):648–651.

Verheggen, B., Cozic, J., Weingartner, E., Bower, K., Mertes, S., Connolly, P., Gallagher, M., Flynn, M., Choularton, T., and Baltensperger, U. (2007). Aerosol partitioning between the interstitial and the condensed phase in mixed-phase clouds. Journal of Geophysical Research: Atmospheres, 112(D23).

Wallace, J. M. and Hobbs, P. V. (2006). Atmospheric science: an introductory survey, volume 92. Elsevier.

Wang, P. K. (2013). Physics and dynamics of clouds and precipitation. Cambridge University Press.

Weitkamp, C. (2006). Lidar: range-resolved optical remote sensing of the atmosphere, volume 102. Springer Science & Business.

Wu, Y., Liu, D., Wang, J., Shen, F., Chen, Y., Cui, S., Ge, S., Wu, Y., Chen, M., and Ge, X. (2019). Characterization of size-resolved hygroscopicity of black carbon-containing particle in urban environment. Environmental Science & Technology, 53(24):14212–14221.

Yau, M. K. and Rogers, R. R. (1996). A short course in cloud physics. Elsevier.

Yuan, T., Li, Z., Zhang, R., and Fan, J. (2008). Increase of cloud droplet size with aerosol optical depth: An observation and modeling study. Journal of Geophysical Research: Atmospheres, 113(D4).

Zhai, J., Lu, X., Li, L., Zhang, Q., Zhang, C., Chen, H., Yang, X., and Chen, J. (2017). Size-resolved chemical composition, effective density, and optical properties of biomass burning particles. Atmospheric Chemistry and Physics, 17(12):7481.

Zhang, R., Li, G., Fan, J., Wu, D. L., and Molina, M. J. (2007). Intensification of pacific storm track linked to asian pollution. Proceedings of the National Academy of Sciences, 104(13):5295–5299.

Zhang, Z. and Moore, J. C. (2014). Mathematical and physical fundamentals of climate change. Elsevier.

Zhao, C., Qiu, Y., Dong, X., Wang, Z., Peng, Y., Li, B., Wu, Z., and Wang, Y. (2018). Negative aerosol-cloud re relationship from aircraft observations over hebei, china. Earth and Space Science, 5(1):19–29.

Zieger, P., Fierz-Schmidhauser, R., Weingartner, E., and Baltensperger, U. (2013). Effects of relative humidity on aerosol light scattering: results from different european sites. Atmospheric Chemistry and Physics, 13(21):10609.